## The genesis of the Ashram REE deposit, Quebec: insights from

## bulk-rock geochemistry, apatite-monazite-bastnäsite

## replacement reactions and mineral chemistry

Caitlin M.J. Beland and Anthony E. Williams-Jones

McGill University

8 Abstract

Growing demand for the rare earth elements, particularly the heavy REE (HREE), has fuelled a boom in mineral exploration and scientific research on carbonatite-hosted deposits, especially those with unusual HREE enrichment. The Ashram REE deposit is a carbonatite-hosted REE deposit showing HREE enrichment above a central fault breccia. Magmatic processes were important in the genesis of the deposit, but hydrothermal remobilization was crucial for the concentration of the REE to potentially economic levels and fractionation of HREE.

The REE minerals in the Ashram deposit were precipitated from hydrothermal fluids. They comprise monazite-(Ce) and bastnäsite-(Ce), with lesser monazite-(Nd) and trace xenotime-(Y) and aeschynite-(Nd). This mineralization occurs as disseminations in breccia matrices, in veins, and as vug fillings. Monazite-(Ce) was the earliest mineral to form, followed by xenotime-(Y) and bastnäsite-(Ce). The composition of monazite-(Ce) varies with location in the deposit. In particular, it is preferentially enriched in the LREE with increasing distance from the fault breccia. This enrichment is attributed to a combination of cooling and decreased pH buffering of the fluid in the breccia, which is interpreted to have been the conduit for fluids. Xenotime-(Y) composition does not vary with location, indicating that the fluid did not fractionate the HREE from one another. Instead, the fluid leached HREE from earlier minerals, namely fluorite, carbonates and huttonite, and deposited them *in situ* as xenotime-(Y) upon contact with a source of phosphate. Bastnäsite-(Ce) replaced monazite-(Ce) through ligand exchange (F-, CO<sub>3</sub><sup>2-</sup> for PO<sub>4</sub><sup>3-</sup>), while preserving the original REE chemistry. Interaction of a compositionally evolving fluid with host rocks of variable bulk composition and buffering capacity resulted in deposit-scale fractionation and zonation of the REE.

1 Introduction

2

3

4

5

6

7

8

9

10

11

12

13

14

15

16

17

18

19

20

21

22

23

24

25

26

27

28

29

Carbonatites are an important source of rare earth elements (REE), particularly the light REE (LREE). The Mountain Pass carbonatite (USA) was responsible for virtually all global REE production from 1965 until 1986, when the Bayan Obo deposit (China) came on stream, making it unprofitable to continue mining at Mountain Pass (Castor and Hedrick, 2006). Based largely on studies of the Mountain Pass deposit, carbonatite-hosted REE ores have long been considered as magmatic (Olson et al., 1954; Mariano, 1989; Castor, 2008). Recent studies, however, have proposed an integrated magmatic-hydrothermal model for a number of carbonatite-hosted REE deposits, including Jacupiranga (Costanzo et al., 2006) and Barra do Itapirapua, Brazil (Ruberti et al, 2008); Amba Dongar, India (Doroshkevich et al., 2009); Maoniuping, China (Xie et al., 2015); Bear's Lodge, USA (Moore et al., 2015); Montviel, Canada (Nadeau et al., 2015); Wicheeda, Canada (Trofanenko et al., 2016); and Palabora, South Africa (Giebel et al., 2017). According to these studies, hydrothermal fluids of magmatic origin play an essential role in concentrating the REE to potentially economic levels, either by transferring them directly from the magma and/or by leaching and remobilizing them from primary minerals. For some deposits, e.g., Bayan Obo, China (Smith et al., 2015) and Karrat Isfjord, Greenland (Mott et al., 2013), it has been proposed that carbonatite-derived fluids transported the REE and deposited them in unrelated country rock. Despite the considerable body of evidence that has been collected in support of a role for hydrothermal fluids in the formation of carbonatite REE deposits, debate continues over the relative importance of hydrothermal and magmatic processes in the concentration of the REE.

Although transport of the REE by carbonatite-derived hydrothermal fluids has commonly been inferred, there are few cases where this has been demonstrated unambiguously. Such unequivocal evidence has been provided by REE daughter minerals (e.g., burbankite) in primary fluid inclusions from the Chilwa Island carbonatite, Malawi (Dowman et al., 2017) and by crushleach analyses of quartz-hosted fluid inclusions from the Kalkfeld and Okurusu carbonatites reporting up to 3 wt% ΣREE (Bühn and Rankin, 1999; Bühn et al., 2002). There is, however, a growing body of experimental evidence that the REE can be transported in appreciable concentrations in aqueous solutions at elevated temperature (e.g., Gammons et al., 2002; Migdisov and Williams-Jones, 2008; Migdisov et al., 2009). This transport is thought to occur

through the complexation of the REE with chloride and sulfate ions. Carbonate, phosphate and fluoride ions are considered depositional ligands (Williams-Jones et al., 2012; Migdisov et al., 2016), in part due to the fact that REE-fluorocarbonates, and to a much lesser extent, monazite, are common ore minerals of the REE in carbonatite-hosted REE deposits (both minerals are relatively insoluble in aqueous fluids; Migdisov et al., 2016), and that apatite and fluorite are extremely common gangue minerals.

In the majority of carbonatite-hosted REE deposits, REE-fluorocarbonates are the principal ore minerals, although in some there is significant REE-phosphate mineralization in the form of monazite, e.g., Phalaborwa, South Africa (Giebel et al., 2017). In deposits containing both mineral groups, there is an 'antipathic' relationship, or strong spatial separation between the REE-fluorocarbonates and the REE-phosphates, first recognized by Kapustin (1971). Although parageneses involving these two families of REE minerals have been documented, the factors responsible for the antipathic relationship between them have rarely been investigated (Giebel et al., 2017).

Among the many questions that remain regarding LREE mineralization in carbonatites, the origin of rare occurrences of heavy REE (HREE) mineralization in these rocks may be the most puzzling. Owing to their generation from mantle melts, carbonatites are innately LREE-rich (Pell, 1996) and several studies have shown that carbonatite-derived hydrothermal fluids are dominated by the LREE (e.g. Bühn and Rankin, 1999). There are, however, rare occurrences of carbonatite-derived hydrothermal deposits or parts of such deposits that are highly enriched in the HREE, e.g., Lofdal, Namibia (76.3 % heavy rare earth oxide (HREO) / total rare earth oxide (TREO), Bodeving et al., 2017) and Chilwa Island (Dowman, 2014), respectively. Models for their formation have ranged from late-stage magmatic enrichment of the HREE in Fe-rich residua (Dowman et al., 2017), to fractionation of the HREE during exsolution of carbonatite-derived fluid (Bühn, 2008), and preferential immobilization of the HREE (Smith et al., 2018) due to the weak pH buffering capacity of the host rocks (Williams-Jones et al., 2015).

The Eldor Carbonatite Complex and its Ashram REE deposit provide a rare opportunity to explore the relative importance of magmatic and hydrothermal processes in carbonatite-related REE ore formation, the controls on REE-phosphate deposition and the processes by which the REE

may be fractionated in carbonatitic environments. This is because, although the dominant REE mineral in the Ashram deposit is monazite, the deposit contains several REE minerals that are spatially separated on a deposit-scale and there is an unusual zone of middle REE (MREE; Sm, Eu, Gd) and HREE enrichment.

In this contribution, we use textural observations of the REE minerals and associated phases to establish a mineral paragenesis for the Ashram deposit and report the major and trace element compositions of these minerals. Variations in the latter are evaluated in the context of deposit-scale bulk geochemical trends and changes in lithology that have been modelled in three dimensions. Based on the results of this research, we have developed a model in which a syntectonic, multi-stage magmatic carbonatite evolution laid the groundwork for carbonatite-derived REE-bearing fluids to rework primary mineral assemblages, and deposit REE minerals in response to the cooling and differential buffering of the fluid during its interaction with the host rock.

Geology of the Eldor Carbonatite Complex

The Eldor carbonatite complex is located approximately 130 km south of Kuujjuaq, in northern Québec, Canada (Fig. 1). It is hosted by rocks of the Labrador Trough, which is the foreland of the New Quebec Orogen, a Paleoproterozoic fold and thrust belt on the eastern margin of the Superior Province (Clark and Wares, 2006). The Labrador Trough is an early Proterozoic rift basin that experienced three cycles of volcanism and sedimentation, separated by erosional unconformities (Clark and Wares, 2006). The Eldor carbonatite was emplaced at the end of the second cycle of rifting, within the volcanosedimentary Murdoch Formation. Although the emplacement age of the carbonatite is unknown, it is constrained to be younger than  $1870 \pm 4$  Ma by the U-Pb age of a rhyodacite of the Murdoch Formation, which it crosscuts (Machado et al., 1997). The complex was subsequently deformed and metamorphosed to greenschist facies during the Hudsonian Orogeny (1.82 - 1.77 Ga) (Clark and Wares, 2006).

Commerce Resources Corp. is currently exploring the Eldor carbonatite complex and has reported measured and indicated resource estimates of 29.3 Mt at 1.90 % TREO, using a cut-off grade of 1.25 % TREO (Gagnon et al., 2012). The carbonatite is exposed in a 7 x 3.5 km elliptical area and comprises a suite of intrusions ranging in composition from calcite- through dolomite-

to ferro-carbonatite. Based on the distribution of the REE, the pluton has been subdivided into a Rim composed of REE-poor calcite- and dolomite-carbonatite and a core of dolomite carbonatite and ferrocarbonatite that hosts the Ashram REE deposit (Fig. 2A). Exposure in the area is poor, and the bulk of the Ashram deposit lies beneath a pond. As drilling has focussed on the REE-mineralized zones, the relationships among the various units are not well known, especially the contact between the Ashram deposit and the outer part of the carbonatite. For example, the outermost unit of the Ashram deposit is typically in contact with calcite carbonatite, but its contact with the Rim dolomite carbonatite has not been observed and is inferred. The Ashram deposit is separated from greenstones on its west side by fenites (phlogopitite and arfvedsonite-albitite), the outer limit of which has not been intersected in drilling. To date, drilling has been insufficient to elucidate the subsurface orientation of both the deposit and the complex. Research on Ashram has been limited to an unpublished M.Sc thesis, which provided a general description of the deposit (Schmidt, 2013) and a paper describing the mineralogy and paragenesis (Mitchell and Smith, 2017).

The Rim is comprised of two types of calcite carbonatite and a dolomite carbonatite. Calcite carbonatite 1 is fine grained and finely banded in apatite, magnetite, and phlogopite, with late calcite. This assemblage persists into the coarser grained calcite carbonatite 2, though this unit also contains appreciable pyrochlore. Dolomite carbonatite is the latest Rim lithology and is fine grained with the same non-carbonate mineral assemblage as calcite carbonatite 2, with the addition of fluorite.

The Ashram deposit comprises three main zones of mineralization, namely the BD, B, and A zones (Fig. 2). In addition, there is a largely unmineralized breccia (Fig. 2B). The outermost BD zone is a fluorapatite-rich, dolomite carbonatite with REE fluorocarbonate mineralization (bastnäsite-(Ce) (REECO<sub>3</sub>F), parisite-(Ce) ( $Ca(Ce,La)_2(CO_3)_3F_2$ ), synchisite-(Ce) ( $CaCe(CO_3)_2F$ )) grading 0.6 - 1.0 wt % TREO (Fig. 3A,B). This unit is extremely rich in phosphate, with an average of 7 vol % apatite and up to 14 wt %  $P_2O_5$  (Fig. 3B). The B zone is also a dolomite carbonatite, but with a dominant assemblage of fluorite (4 vol %) + monazite (REEPO<sub>4</sub>) and a grade of 1 - 2 wt % TREO (Fig. 3C). This assemblage continues into the ferroan dolomite carbonatite of the innermost A zone, which is even more enriched in F and REE, with an average fluorite content of 8 vol % and

2

3

4

5

6

7

8

9

10

11

12

13

14

15

16

17

18

19

20

21

22

23

24

25

26

27

28

29

a grade of 1 - 3+ wt % TREO (Fig. 3D). Rocks intersected in some drill holes appear to have characteristics transitional between those of the A and B zones, and have accordingly been termed A/B. Intervals of these rocks are included as a subdivision of the A zone in maps and resource models. The A zone also contains the MHREO zone, which is a ferrocarbonatite containing monazite-(Nd), subordinate monazite-(Ce), xenotime-(Y) (YPO<sub>4</sub>), and trace aeschynite-(Nd) ((Nd,Ca,Fe)(Ti,Nb)<sub>2</sub>(O,OH)<sub>6</sub>, Mitchell and Smith, 2017). This latter zone is relatively poor in fluorine, containing only minor fluorite, and has a lower REE grade of 1.6 wt % total REE oxides (TREO) on average. For the most part, it occurs near the top of the A zone (<100 m depth) as discontinuous veins, pods and lenses of varying apparent thickness but generally less than a few metres in width. The latest lithotype in the Ashram deposit is a polymictic breccia, most commonly in contact with the BD zone. It is composed of a fine-grained dolomitic matrix with clasts of local provenance, including greenstone, Na- and K-fenites, barren carbonatite and REEmineralized BD zone material (Fig. 3E). Rarely, the matrix contains REE-fluorocarbonate mineralization. The breccia is highly variable in texture and may be matrix- or clast-supported. Locally, it is expressed as a crackle breccia, with little to no matrix carbonate and abundant phlogopite veinlets. In contrast, some intersections are composed of up to 80% matrix, and are strongly sheared. All Asham lithologies are deformed but vary in style and intensity. Localized domains of strongly foliated material are intercalated with massive material on a scale ranging from centimetres to several metres. Foliation is most strongly expressed through textures of apatite and the REE fluorocarbonates in the BD zone (Fig. 3A,B), and fluorite in the B and A zones (Fig. 3C,D).

Examination of intersections of the breccia unit in three dimensions suggests that it is a roughly cone or funnel-shaped feature, occurring mainly along the inner margin of the P<sub>2</sub>O<sub>5</sub>-rich BD zone (Fig. 4A), with REE mineralization mostly located in the interior of the breccia cone (Fig. 4B). Numerous intersections along the western contact of the Ashram carbonatites and the fenitized wall-rock are aligned, suggesting a flattening, or planar side of the cone (Fig. 4), with an orientation of approximately 315/60. Interestingly, rocks with a high (> 10 %) proportion of MREE and HREE are intersected in the hanging-wall, directly above the plane, and whole-rock compositions are increasingly LREE-rich with increasing distance from it (Fig. 4C). It should be

noted that the peripheral intersections with a high proportion of MREE and HREE (Fig. 4C) are unmineralized (Fig. 4B) and this apparent enrichment is likely the signature of silicate minerals in the wall-rock which preferentially accommodate the HREE though at low levels, such as amphibole (e.g. Siegel et al., 2017).

Geochemically, the Eldor Carbonatite Complex is concentrically zoned (Table 1). Within the Ashram deposit, the TREO grade increases towards the center of the deposit from 0.5 to > 3 wt %, and then drops to ~ 1.6 wt % TREO in the innermost MHREO zone. Significantly, this zone is enriched in MREE and HREE, with up to 20% MHREE/TREE, whereas the A, B and BD zones are all LREE-enriched. There is also an iron-enrichment trend towards the center of the deposit, expressed by the dominant carbonate mineral, from dolomite in the outermost BD zone, to ferroan dolomite in the A zone and siderite in the MHREO zone. All the Ashram rocks are P-and F-rich, but there is a distinct mineralogical change in the host of these elements between the BD zone and the rest of the deposit. In the BD zone, the principal phosphate mineral is apatite, whereas P is hosted primarily in monazite-(Ce) in the B and A zones, and monazite-(Nd), monazite-(Ce) and xenotime-(Y) in the MHREO zone. Similarly, the main fluorine phases in the BD zone are the REE fluorocarbonates, but in the B, A and MHREO zones, fluorite is the principal host for fluorine.

19 Methods

Bulk rock chemical data were supplied by Commerce Resources Corp. from their database of Ashram drill core assays, which were performed by Activation Laboratories in Ancaster, Ontario, and comprised all major elements and a large number of trace elements, including the full set of REE. All the samples were ground to 95% -200 mesh and aliquots of each powder fused with lithium metaborate/tetraborate, followed by analysis using inductively coupled plasma optical emission spectrometry (ICP-OES) for the major elements and mass spectrometry (ICP-MS) for the trace elements. The loss on ignition (LOI) was determined after fusion. Samples (1 g) were heated in an oven at 1000°C for 1 h, cooled then weighed, with the percent loss calculated from the difference in weight before and after heating. The fluorine content was determined from 0.2 g samples fused with lithium metaborate/tetraborate in a furnace to release a F<sup>-</sup> ions from the

sample into a solution, which was then analysed using an ion sensitive electrode.

Samples were examined petrographically using a combination of optical and scanning electron microscopy (SEM) and cold-cathodoluminescence (CL). A Hitachi SU5000 SEM, equipped with an Oxford Instruments X-Max<sup>N</sup> 80 silicon drift detector was used for back-scattered electron (BSE) imaging, mineral identification and energy-dispersive X-ray mapping. Cathodoluminescence was required to identify different generations of fluorite, fluorapatite and dolomite, and was carried out using a Reliotron III electron source, operated at 9 kV and 350 nA, and a 3 s exposure time.

Mineral compositions were measured in the Department of Earth and Planetary Sciences at McGill University using a JEOL JXA-8900L electron microprobe equipped with five wavelength-dispersive spectrometers and an Si(Li) energy-dispersive spectrometer. For calcite, dolomite and siderite, spot analyses were conducted at 15 kV with a 20 nA beam current using wavelength-dispersive spectrometry. Spot analyses of apatite, monazite, bastnäsite, xenotime and huttonite were conducted at 20 kV and a 30 nA beam current. All analyses were performed with a 10  $\mu$ m beam diameter. Data reduction was carried out using a ZAF correction procedure. The standards used, the counting times and the detection limits for each element in each mineral are reported in Table 1A.

Trace element concentrations in apatite, fluorite and carbonate minerals were analysed with a laser ablation inductively-coupled plasma mass spectrometer (LA-ICP-MS). Analyses were performed at McGill University using a NewWave 213 nm ND-YAG laser, operated at a fluence of 12 J/cm² for apatite, and 7 J/cm² for fluorite and carbonate minerals. Spots were analysed with a 30s laser warm-up, 45s ablation and 30s washout. In the case of apatite, the spots were 30  $\mu$ m in diameter, and for fluorite and carbonate minerals were 80  $\mu$ m in diameter. The aerosols were transported into a FINNIGAN iCapQ ICP-MS. The dwell time was 20 ms for the REE. Blocks of  $\leq$  15 analyses were collected, bracketed by two analyses of the external standard SRM NIST 610, to apply a linear instrument drift correction. Element concentrations were determined using the software lolite (Paton et al., 2011). The internal standards were the Ca content obtained by electron microprobe analysis for apatite, calcite and dolomite, and the stoichiometric Ca content for fluorite. Siderite analyses were standardized using the Fe content obtained by electron

microprobe analysis.

Carbonate minerals from each lithofacies of the complex were analyzed for their stable carbon ( $^{12}$ C,  $^{13}$ C) and oxygen ( $^{16}$ O,  $^{18}$ O) isotope ratios at the McGill University/Geotop Stable Isotope Laboratory, using a Nu Instruments Perspective isotope ratio mass spectrometer. A total of 94 powdered carbonate samples ( $^{50-100}$  µg) were collected using a handheld drill. An effort was made to sample coarse- and fine-grained minerals separately in rocks with variable grain size. The carbonate powders were dissolved in orthophosphoric acid at  $^{70}$ C and the resulting  $^{60}$ C gas was analyzed via dual inlet following double distillation. Carbon isotope ratios were standardized to Vienna-Pee Dee Belemnite (V-PDB) and are reported as  $^{61}$ C values. Oxygen isotope ratios were standardized to Vienna-Standard Mean Ocean Water (V-SMOW) and are reported as  $^{61}$ O values. On the basis of regular analyses of an in-house standard (UQ6), the reproducibility is considered to be better than 0.05% for both the C and O isotope ratios.

A simple thermodynamic model was constructed to simulate hydrothermal alteration of carbonatites by an acidic solution in a one-dimensional column of rock which was evaluated using a step-flow reactor approach ("box-model"). In our model, the solution is gradually cooled to simulate increased distance from the fluid input zone. During the initial event, a 1 kg aliquot of the initial fluid was equilibrated with 1 kg of fresh rock, altering it and producing a new fluid, which was subsequently equilibrated with another 1 kg of fresh rock at a lower temperature (T-10°C). The process was repeated until the final temperature of 150°C was reached, creating a column of rock altered by the first passage of fluid ("initial pulse"). After the initial pulse, a new aliquot of fluid (1 kg) of the same initial composition, was flushed through the altered column in the same manner as described above ("2<sup>nd</sup> pulse"). This procedure was repeated for 10 pulses. The model was formulated using the HCh/Unitherm code (Shvarov and Bastrakov, 1999). A full list of aqueous species and solids used in the calculations, equations of state used to extrapolate their properties to elevated temperature, and the data sources, is provided in the electronic supplementary data.

1 Results

Bulk Lithogeochemistry

Assays values were weighted by multiplying by their lengths and median values were then calculated for the major oxide and trace element compositions of the Rim carbonatites, Ashram zones and the breccia, given in Table 2. The evolutionary index Ba/(Ba+Sr) (Gomide et al., 2016) was applied to the Eldor carbonatite complex to evaluate relationships between lithofacies. A series of binary plots of the weighted median values of selected components from each mineralized Ashram zone and the Rim carbonatites are given in Fig. 5. For several of the components, the different lithologies define two trends, the first comprising the Rim carbonatites, and the second group comprising the B, A/B, A, and MHREO zones, with the BD zone lying at the intersection of the two trends. Rim samples define a trend towards the BD zone of decreasing Ba/(Ba+Sr), whereas from the BD zone to the inner-most MHREO zone, there is a trend of increasing (Ba/Ba+Sr). Similar trends are observed for other chemical components including P<sub>2</sub>O<sub>5</sub>, Na<sub>2</sub>O, Zn, and TREE, except that for the latter, the MHREO zone lies off-trend at lower values (Fig. 5C).

17 Petrographic Observations

Primary assemblages and textures dominate the mineralogy of the Eldor calcite carbonatites (Rim units). All other units exhibit variable but significant evidence of postmagmatic effects including low strain recrystallization, deformation, and hydrothermal overprinting in the form of secondary features such as veins and vug infill. Textures in carbonate minerals provide an exceptional record of these processes. Breccias are common, especially in the BD and MHREO zones. In the BD zone, coarse angular clasts of early dolomite (bright red in CL) sit in a matrix of fine grained ferroan dolomite (no CL response) (Fig. 6A, B). The same relationship between angular clasts of dolomite and fine grained ferroan dolomite also occurs in the Rim dolomite carbonatite, but clasts are only rarely preserved (Fig. 6C). Siderite of the MHREO zone is brecciated and clasts show multiple episodes of overprinting (Fig. 6D-F). Carbonate textures in the B and A zones are much more variable. In both zones, the carbonate groundmass commonly ranges from a fine to medium

2

3

4

5

6

7

8

9

10

11

12

13

14

15

16

17

18

19

20

21

22

23

24

25

26

27

28

29

grained and nearly equigranular mosaic-texture (Fig. 7A), to weakly to strongly foliated and banded with other minerals including monazite and fluorite (Fig. 7B, and "schlieren carbonatites", Mitchell and Smith (2017)). These two textural end-members may be separated into domains on a fine scale (<1 cm) (Fig. 7C) or crosscut one another. Within a given textural domain, groundmass carbonate minerals commonly show multiple episodes of replacement (Fig. 7D,E). Secondary carbonates may be homogenous or display complex internal textures (Fig. 6C, Fig. 7E) and occur in vugs or veins ± fluorite ± quartz (Fig. 6D,F; Fig. 7B,C). Vug carbonates occur in all Ashram zones, though most commonly in the A and MHREO zones.

Fluorite and apatite are major minerals in the Eldor carbonatite. Apatite is an important component of all the Rim lithologies and the BD zone, but occurs in only trace proportions in the B, A and MHREO zones. In the Rim carbonatites, apatite is a coarse-grained, primary mineral with an ovoid crystal shape (Fig. 6C), and blue-violet color in CL (Fig. 8A), mantled locally by finegrained, pale violet to pale pink (CL) apatite (Fig. 8A). In the BD zone, the apatite is fine-grained and sucrosic, commonly with irregular grain boundaries, and is pale pink in CL (BD-s apatite), locally with pale violet domains (Fig. 8A). Apatite in this zone is commonly spatially associated with the REE-fluorocarbonates. In the B zone, the apatite is fine- to medium-grained, crystalline or sucrosic and white to pale grey-violet in CL (Fig. 8B). Rarely, it is intergrown with thin bands of fine-grained monazite and dolomite (Fig. 8C). There are two types of apatite in the A zone. Medium-grained ovoid primary apatite (A-p type) with a pale blue CL color is extremely rare, and mantled by the more common very fine-grained, sucrosic apatite (A-s type) with a yellow-white color in CL (Fig. 8D). Both B and A-s type apatite varieties are commonly intergrown on a very fine scale with royal blue (CL) fluorite (Fig. 8B,D,E). Fluorite occurs in the innermost (latest) Rim units and the BD zone, but is most abundant in the B and A zones. There are three varieties of fluorite, distinguished by their CL color, namely bright green, blue-green, and royal blue varieties (Fig. 8F). All three varieties are strongly associated spatially with monazite-(Ce) (or bastnäsite-(Ce) in the BD zone). Bright green and blue-green (CL) fluorite occur in the B, A and MHREO zones, whereas fluorite in the BD zone is exclusively royal blue in color (CL). Indeed, across the deposit, all fluorite in contact with apatite displays a royal blue color in CL (e.g. Fig. 8B). The relative timing of the different fluorite varieties is unclear. In some cases, bright green fluorite appears to have been

earlier than blue-green fluorite, and vice versa, or rarely the fluorite displays oscillatory zoning of the two CL colors.

1

2

3

4

5

6

7

8

9

10

11

12

13

14

15

16

17

18

19

20

21

22

23

24

25

26

27

28

29

The REE minerals, monazite-(Ce), bastnäsite-(Ce), parisite-(Ce), synchysite-(Ce), xenotime-(Y) and aeschynite-(Nd) occur in veins, as vug fillings, and as disseminations in breccia matrices in all Ashram zones (Fig. 9). Monazite-(Nd) has been observed exclusively in the MHREO zone, where it occurs at the margins of siderite crystals (Fig. 9A). Monazite-(Ce) is, spatially, strongly associated with fluorite (Fig. 9B). The different P- and F-bearing minerals are rarely observed in contact with each other, due to the distinct change in mineralogy from the BD zone to the rest of the Ashram deposit. Where they are in contact, the REE-fluorocarbonates invariably mantle monazite-(Ce) (Fig. 9C,D). Rarely, monazite-(Ce) and bastnäsite-(Ce) may appear to be intergrown (Mitchell and Smith, 2017, their Fig. 20) as shown on comparative EDS maps of P and Ce, however it is noteworthy that there are very fine (1 µm) P-bearing inclusions within the bastnäsite-(Ce) domains, and the bastnäsite-(Ce) domains surround or border monazite-(Ce). Xenotime-(Y) is generally found in association with monazite-(Ce), where it mantles the latter (Fig. 9E,F). In some MHREO zone samples, very fine-grained xenotime-(Y) is included in fractured, patchily altered crystals of huttonite (Fig. 9F). Where apatite and monazite-(Ce) are observed in contact, monazite-(Ce) mantles apatite (or may poikilitically enclose it, Mitchell and Smith (2017)), occurs in fractures within or at grain boundaries of the latter (Fig. 9C,D), or rarely, occurs in bands with fine grained dolomite within recrystallized apatite (Fig. 8C). Aeschynite-(Nd) is commonly associated with, and later than, monazite-(Ce), xenotime-(Y), and Nb-Ti oxides. Bastnäsite-(Ce), monazite-(Ce) and -(Nd), and aeschynite-(Nd) are typically homogenous and unzoned, whereas xenotime-(Y) crystals vary and locally show oscillatory zoning. Very rarely, monazite-(Ce) crystals display a core-rim morphology, where cores are Th-rich and La-poor relative to rims (Fig. 10C-F).

Other minerals present in significant proportions in our samples of the Ashram deposit are pyrite, sphalerite, magnetite and bafertisite (MHREO only), quartz, phlogopite, and barite. Pyrite is a ubiquitous accessory mineral in Ashram carbonatites typically associated with dolomite. Concentrations of pyrite are locally higher in the MHREO zone, where it occurs with sphalerite and magnetite in strong association with dolomitization of siderite and magnesian siderite (Fig. 6F) and was deposited before REE minerals (Fig. 7C). Quartz also occurs in all zones

as blebs and in late, undeformed veins ± fluorite ± carbonate. The MHREO zone is particularly rich in quartz where it occurs in vugs with dolomite (Fig. 6D,F). All Ashram units contain phlogopite in veins that are commonly deformed (folded) (Fig. 7C) and are variably associated with monazite-(Ce) and xenotime-(Y), or bastnäsite-(Ce). Where in contact with REE minerals, the latter are interstitial to phlogopite, or in some cases, veins of monazite-(Ce) + fluorite + dolomite crosscut phlogopite (Fig. 10A). Bafertisite (Ba<sub>2</sub>Fe<sub>4</sub><sup>2+</sup>Ti<sub>2</sub>(Si<sub>2</sub>O<sub>7</sub>)<sub>2</sub>O<sub>2</sub>(OH)<sub>2</sub>F<sub>2</sub>) is an accessory mineral exclusive to the MHREO zone, where it occurs in late veins relative to monazite mineralization, in close association to magnetite, and is commonly altered to barite (Fig. 10B). Barite has also been rarely observed as prismatic crystals in close association with phlogopite in vugs in the BD zone. Magbasite (KBaFe<sup>3+</sup>Mg<sub>7</sub>Si<sub>8</sub>O<sub>22</sub>(OH)<sub>2</sub>F<sub>6</sub>) in the MHREO zone was reported by Mitchell and Smith (2017) but was not observed in our samples. Similarly, microcline has been reported as a trace phase associated with phlogopite and quartz in the BD zone (Mitchell and Smith, 2017) though we have not observed it. The deposit is host to a variety of rare accessory and trace minerals, chiefly secondary Ba- and Be- bearing phases unrelated to REE mineralization. For further information readers are referred to Mitchell and Smith (2017).

16 Mineral Chemistry

Carbonates: Electron microprobe analyses were performed on carbonate minerals in samples collected from each lithofacies of the carbonatite complex, and representative compositions are given in Table 3. Given the complexity of textures demonstrated above, carbonate minerals in different samples of a zone may record only some of the compositional changes (or potentially different trends in composition) than those presented in the following. Calcite from the earliest Rim calcite carbonatite has a near end-member composition with minor Fe, Mg, Mn, and Sr. The later generation of primary calcite (calcite carbonatite 2) is enriched in Sr, Al, and Ba, and depleted in Mn, relative to the former. Generations of dolomite from the Rim dolomite carbonatites are progressively depleted in Sr and enriched in Fe, and variably enriched and depleted in Mn and Ba (Fig. 6C). In the BD zone, Fe and Mn are enriched and Sr and Ba are depleted in dolomite 2 relative to dolomite 1. The latest dolomite generation is depleted in Fe and Mn and enriched in Sr, Ba, and Al relative to dolomite 2 (Fig. 6B). Dolomites of the B zone are progressively enriched in Fe and Mn and depleted in Al and Ba (Fig. 7E). Groundmass carbonate compositions of the A zone

2

3

4

5

6

7

8

9

10

11

12

13

14

15

16

17

18

19

20

21

22

23

24

25

26

27

28

29

are variable, with up to five generations in a sample. Early ferroan dolomite is replaced by an Fe-Mn-poor, and Sr-Ba-Al-enriched dolomite, which is then replaced by ferroan dolomite depleted in Sr, Ba, and Al, relative to the second generation. There is further Fe and Ba enrichment with the replacement of dolomite by magnesian siderite (Fig. 7D). In contrast, MHREO carbonates display progressive depletion of Fe and enrichment of Mg, with early siderite replaced by increasingly Mg-rich compositions (Fig. 6D)Fig. 6. Compositions of secondary carbonates are just as variable as their groundmass counterparts, and selected examples are provided in Table 3. In one A zone vug, dolomite compositions record variable enrichment and depletion in Fe, Mn, Sr, and Al. Secondary dolomite in vugs in the MHREO zone record Fe-Mn enrichment towards ankerite, with variable enrichment in Sr and Ba.

Carbonates of each lithofacies were also analysed by LA-ICP-MS for their trace element compositions (Table 4). Calcite and dolomite from the Rim and BD zones contain highly variable Sr over consistently low (< 50 ppm) Zn, whereas dolomite from the A zone, most analyses from the B zone, and vug dolomite contain variable Zn over relatively low Sr (Fig. 11A). All calcite and most dolomite compositions have Y/Ho ratios within the primary range delineated by Chakhmouradian et al. (2017) (Fig. 11B). Exceptions are some analyses of groundmass ferroan dolomite from the Rim dolomite carbonatite, and dolomite from the breccia unit. In contrast, many dolomite analyses from all Ashram units and the breccia lie outside the primary field of  $Eu/Eu^*$  ( $Eu_{CN}/(0.5^*(Sm+Gd)_{CN})$ ) and  $Ce/Ce^*$  ( $Ce_{CN}/(0.5^*(La+Pr)_{CN})$ ) along with vug dolomite (Chakhmouradian et al., 2017; Fig. 11C). Analyses from each lithofacies form linear trends in their REE contents and LREE-enrichment (chondrite-normalized La/Yb), with the exception of the dolomite from the breccia unit, which clusters with low REE contents and is LREE-depleted (Fig. 11D). Siderite was not included in Fig. 11 because its trace element composition is not directly comparable to calcite and dolomite due to the much smaller Fe site. However, it is worth noting that siderite from the MHREO zone is Zn-rich (≤ 619 ppm) (Table 4). Siderite Y/Ho, Eu/Eu\*, and Ce/Ce\* are within the same ranges defined by calcite and dolomite, though REE abundances are very low ( $\leq$  43 ppm REE) and HREE-enriched (La/Yb = 0.03 – 0.47) (Table 4). Apatite: Despite their striking difference in morphology and CL color, all varieties of apatite

classify as fluorapatite based on their fluorine content, and contain similar proportions of most

2

3

4

5

6

7

8

9

10

11

12

13

14

15

16

17

18

19

20

21

22

23

24

25

26

27

28

29

major and minor elements, except for Sr. Representative compositions analyzed by EMPA are provided in Table 2A. The apatite varieties are best distinguished by their trace element contents and the average compositions for each variety are provided in Table 5. All coarse-grained apatite ovoid in shape (primary) contains lower Sr and Ba than fine-grained apatite varieties with a recrystallized texture (Fig. 12A). Primary Rim and BD apatite also contain less Na than the other Ashram apatite types (Table 5). Secondary A zone apatite (A-s) is the most REE-rich, containing up to 1.7 wt% REE (Fig. 12B). All other varieties overlap considerably in their total REE contents but vary significantly in distribution of the REE (Fig. 12B). Primary Rim and BD zone apatite are strongly LREE-enriched, with La/Yb<sub>CN</sub> ranging from 20 to 100. Primary A zone apatite (A-p) are less LREE-enriched, with La/Yb<sub>CN</sub> ranging from 5 to 20, and all secondary, recrystallized varieties of apatite (Rim-s, BD-s, B, A-s) have flatter distributions with La/Yb<sub>CN</sub> from 1 to 11 (Fig. 12B). Significantly, in cases where two generations of apatite are observed in contact, secondary apatite is depleted in La and Ce, and enriched in REE from Nd and heavier, relative to primary apatite (Fig. 12C, Table 5). Coarse-grained, ovoid apatite have a narrow range in Y/Y\* (Y<sub>CN</sub>/(0.25\*Dy<sub>CN</sub> + 0.75\*Ho<sub>CN</sub>) from 0.63 to 0.80, whereas fine-grained apatite types display wider variations from 0.62 to 1.14 (Fig. 12C). All apatite varieties have  $Eu/Eu^*$  ( $Eu_{CN}/0.5^*$ (Sm+Gd)<sub>CN</sub>) < 1, with a maximum of 0.88 (Fig. 12D). Overall, apatite from the Rim units and primary apatite from the BD zone (violet CL) are similar in their trace element compositions and are distinct from the other varieties of apatite. Primary A zone apatite has a trace element composition more similar to the secondary varieties, despite its igneous texture. However, differences in composition between Ap and A-s types follow the same trends as seen between primary and secondary varieties in other zones. B zone apatite is distinct, and though it shares textural features with secondary varieties (Rim-s, BD-s, A-s) its trace element composition is largely similar to that of primary A zone apatite, and contains much more Sr and Na than all other varieties (Table 5). Fluorite: Fluorite from the Rim dolomite carbonatite, BD zone, MHREO zone, polymictic breccia and late veins (crosscutting mineralization) were analysed by LA-ICP-MS. Their average compositions are reported in Table 6. No data are presented for fluorite from the B and A zones. Owing to the intimate intergrowth of fluorite with monazite-(Ce) in these zones, we were not able to determine fluorite compositions free of a contribution from monazite-(Ce). We note that

2

3

4

5

6

7

8

9

10

11

12

13

14

15

16

17

18

19

20

21

22

23

24

25

26

27

28

29

analyses of A zone fluorite are published in the literature (Mao et al., 2015; Mitchell and Smith, 2017) however, it is unclear from these studies which generation of fluorite was sampled. As demonstrated in Fig. 9B, there are at least two generations of fluorite in the A zone. Nonetheless, these compositions are included in Fig. 13. All the fluorite analysed is relatively pure CaF<sub>2</sub>, with other cations present in trace proportions (Table 6). The fluorite from the different zones is all Yenriched and REE-poor, with TREE contents all below 0.09 wt % (Table 6). Nonetheless it can be divided into two groups on the basis of its REE chemistry (Fig. 13). Fluorite from the Rim and BD zones is the most HREE-depleted relative to the LREE (Fig. 13A) and is characterized by chondritenormalized REE profiles that are essentially flat (Fig. 13B). In contrast, fluorite from the MHREO zone and late veins is strongly enriched in HREE relative to the LREE. These fluorite types are characterized by REE profiles that are steeply positive through the LREE, and flat to negatively sloped through the HREE. Significantly, the fluorite of the MHREO zone is both the richest in TREE and the most HREE-enriched. Fluorite from the polymictic breccia is similarly enriched in HREE (relative to LREE) but has the lowest TREE content of fluorite from the different units (Fig. 13A). Analyses of A zone fluorite from Mao et al. (2015) and Mitchell and Smith (2017) are compositionally similar to fluorite from the MHREO zone and late veins. REE-bearing Minerals: In samples from the B, A and MHREO zones, the compositions of monazite-(Ce) and bastnäsite-(Ce) vary systematically with location in the deposit, particularly in respect to their La and Th contents (Fig. 14). Representative analyses of monazite-(Ce) and bastnäsite-(Ce) from all units are given in Tables 7 and 8, respectively. From the center of the deposit outwards, both minerals display a continuous enrichment in La, and depletion in Th (Fig. 14). Compositions of monazite within a given sample do not vary with the minerals they are associated with, such as fluorite, phlogopite, and xenotime. Instead, monazite compositions within a sample are clustered (Fig. 14A). The BD zone monazite-(Ce) and bastnäsite-(Ce) compositions do not follow these spatial trends, however, and have the lowest La contents of these minerals in all the zones; their Th content completely overlaps that of these minerals in the A zone (Fig. 14). Monazite-(Ce) and bastnäsite-(Ce) display a continuum of compositions from the MHREO zone to the B zone, whereas monazite-(Ce) and bastnäsite-(Ce) from the BD zone form a distinct, off-trend population.

Xenotime was identified in samples from the MHREO, A and B zones. Representative analyses are given in Table 9. All the grains analysed classify as xenotime-(Y), and the concentrations of their major elements do not vary systematically across the deposit (Table 9).

Although not a REE mineral, sensu stricto, altered huttonite (MHREO zone) contains significant proportions of REE, ranging from 5.66 to 23.57 wt % TREO, and is Y(HREE)-dominant (Table 10). Owing to their strongly altered nature, huttonite crystals display extremely variable compositions, and are depleted in  $ThO_2$  and  $SiO_2$ , with concentrations of these oxides ranging from 35.74 to 58.49 wt % and 7.58 to 13.55 wt %, respectively; the stoichiometric  $ThO_2$  and  $SiO_2$  contents are 81.46 wt % and 18.54 wt %, respectively (Table 10). The analytical totals are generally low, ranging from 75.65 to 96.25 %, indicating variable degrees of hydration. Non-formula components (including the REE) are abundant, namely FeO,  $P_2O_5$  and CaO . Typically, analyses with the lowest totals have the highest proportions of non-formula components like CaO and FeO, and the least  $ThO_2$  and  $SiO_2$  (Table 10).

Stable Isotope Geochemistry

Samples of calcite, dolomite and siderite were analysed for their stable carbon and oxygen isotope composition and the values standardized to  $\delta^{13}$ C V-PDB and  $\delta^{18}$ O V-SMOW (Table 3A, Fig. 15). The sample collection method used is coarse (handheld drill) relative to variations in carbonate compositions demonstrated above. Early dolomite cores in the BD zone carbonatites (dolomite 1, red in CL) are visible in rock samples with the naked eye and were sampled separately. Later generations (dolomite 2 and 3, Table 3) are not visibly distinguishable from one another, therefore the 'groundmass dolomite' presented here represents a mixture of these dolomite compositions. The same is true for fine-grained groundmass dolomite of the Rim dolomite carbonatite, and the B and A zones. Siderite isotopic compositions presented here may be a mixture of coarse siderite cores and minor Mg-siderite (e.g. Fig. 6D).

Calcite from the Rim calcite carbonatite has the lightest  $\delta^{13}$ C and  $\delta^{18}$ O values, ranging from -5.44 to -4.49‰, and 7.49 to 9.76‰, respectively. Early BD zone dolomite (red in CL, Fig. 7A) has similar  $\delta^{13}$ C and  $\delta^{18}$ O values, ranging from -4.62 to -3.53‰ and 9.14 to 10.87‰, respectively. All other samples have higher values. The  $\delta^{13}$ C and  $\delta^{18}$ O values of late BD zone groundmass dolomite

range from -3.28 to -2.04‰ and 11.15 to 15.44‰, respectively, whereas groundmass dolomite from the Rim dolomite carbonatite is isotopically heavier, ranging in  $\delta^{13}$ C from -2.09 to -0.49‰ and in  $\delta^{18}$ O from 12.99 to 16.41‰. The  $\delta^{13}$ C and  $\delta^{18}$ O values of B zone dolomite are the most variable, ranging from -3.17 to 0.26‰ and 10.00 to 17.72‰, respectively. In contrast, dolomite from the A zone has more consistent  $\delta^{13}$ C and  $\delta^{18}$ O values. They range from -2.86 to -1.60‰ and from 13.42 to 17.54‰, respectively. Samples of siderite from the MHREO zone also have consistent  $\delta^{13}$ C and  $\delta^{18}$ O values, ranging from -3.73 to -2.49‰ and from 14.88 to 17.09‰. There is a general trend of heavier  $\delta^{18}$ O isotopic values from the Rim towards the center of the complex.

10 Discussion

Magmatic Evolution

1

2

3

4

5

6

7

8

9

11

12

13

14

15

16

17

18

19

20

21

22

23

24

25

26

27

28

At many localities, carbonatite magmas evolved from apatite-rich calcite carbonatite towards Ba-Sr-REE-rich dolomite carbonatite driven by fractionation of apatite, phlogopite and calcite (e.g. Le Bas and Handley, 1979; Bühn and Rankin, 1999; Xie et al., 2009), in some cases towards enrichment in monazite, strontianite and norsethite (Gomide et al., 2016). Overall, bulk rock compositions of the Eldor complex follow this trend of Ba and REE enrichment but are unusual in that Sr is not enriched in the more evolved units (Ashram) (Fig. 5). Trace norsethite occurs as inclusions in fluorite (Mitchell and Smith, 2017) but strontianite is absent. Moreover, textural relationships of most of the monazite mineralization indicate a hydrothermal origin, rather than magmatic crystallization. The exception may be the ptygmatic monazite bands documented by Mitchell and Smith (2017) (their Fig. 31), which these authors interpret as a deformed cumulate layer. These monazite bands form the margins of a band of fluorite, and as such may be alternatively interpreted as part of a hydrothermal assemblage. If Ashram carbonatite magmas did crystallize monazite, it does not represent a significant proportion of the present-day monazite population. We propose that the Eldor carbonatite magmas evolved compositionally in the typical trend towards Ba-Sr-REE enrichment, but this evolution was arrested before significant Sr-enrichment or monazite saturation were reached.

Though Eldor follows the same overall compositional trends as many other carbonatite

2

3

4

5

6

7

8

9

10

11

12

13

14

15

16

17

18

19

20

21

22

23

24

25

26

27

28

29

complexes, there appears to be a break in composition between the Rim-BD zone carbonatites and the interior Ashram (B, A, MHREO) carbonatites (Fig. 5). We propose that there were at least two main stages of carbonatite magma emplacement from an evolving source; one represented by the Rim and BD zones, characterized by high phosphate and low REE content, and a second represented by the B, A, and MHREO zones, characterized by very low phosphate and relatively high REE contents. A two-stage emplacement model is strongly supported by the occurrence of the polymictic breccia at the inner margins of the BD zone. The breccia commonly contains fragments of BD carbonatite and fenitized wall-rock, and spatial relationships suggest that it has an asymmetrically flattened conical shape. As such, we interpret this unit to be an intrusive breccia associated with the emplacement of the Stage 2 carbonatites that host the Ashram REE deposit. Brecciation concomitant with carbonatite emplacement is observed in many complexes (e.g. Heinrich 1966; Le Bas, 1977; Swinden and Hall, 2012; Chakhmouradian et al., 2016a).

Carbonate mineral REE compositions support a two-stage emplacement model. Significantly, the BD zone dolomite and ferroan dolomite have trace element compositions that completely overlap with those of their Rim counterparts, providing further evidence that the BD zone belongs to the first stage of carbonatite emplacement, and is distinct from the inner Ashram units (Stage 2) (Fig. 11). Trends in carbonate REE content relative to LREE-enrichment (La/Yb<sub>CN</sub>) (Fig. 11D) for the Rim and BD zone carbonatites follow those shown for the Aley carbonatites in British Columbia, and can be explained by the effects of other fractionating REE-bearing minerals (Chakhmouradian et al., 2016b). Rim calcite carbonatite 1 contains abundant apatite in layers. This apatite is LREE-rich relative to the HREE (Table 5, Fig. 12B) thus its early crystallization results in calcite with progressively lower REE and (La/Yb)<sub>CN</sub> ratios (Fig. 11D). The slope of this trend is shallower in calcite from Rim calcite carbonatite 2 likely due to the crystallization of pyrochlore, which has an affinity for the LREE (e.g. Hornig-Kjarsgaard, 1998) in addition to apatite. In the Aley calcite carbonatites, this stage is associated with co-crystallization of apatite and monazite (Chakhmouradian et al., 2016b). The slope of the trend further shallows in the Rim and BD zone dolomite carbonatites (Fig. 11D). The same trend is seen in the Aley dolomite carbonatites and is attributed to monazite fractionation. However, no magmatic monazite has been identified in the Rim and BD zone dolomite carbonatites. Rim dolomite carbonatite contains abundant pyrochlore,

2

3

4

5

6

7

8

9

10

11

12

13

14

15

16

17

18

19

20

21

22

23

24

25

26

27

28

29

and primary apatite from the Rim and BD zone dolomite carbonatites is more LREE-enriched than that of the calcite carbonatites (Fig. 12B, Table 5), therefore it is plausible that the observed flattening is due to crystallization of increasingly LREE-rich apatite in these dolomite carbonatites. There is a clear evolutionary trend in carbonate mineral REE compositions that can be related to the fractionation of other phases from the Rim calcite carbonatites through to the BD zone dolomite carbonatite that is identical to that observed in the Aley carbonatites. However, it is significant that the B and A zone dolomite carbonatites do not follow the pattern, which appears to be 'reset' in their carbonate compositions (Fig. 11D), consistent with a two-stage emplacement model. Additionally, compositions of primary apatite from the A zone are distinct from those of the Rim and BD zone carbonatites which cluster together, particularly in respect to their REE distributions (Fig. 12B,C), supporting the hypothesis that there were two magmatic events at Eldor.

The stable C and O isotopic compositions of the carbonate minerals further support a twostage emplacement model. Some calcite crystals from the Rim calcite carbonatites have isotopic signatures that lie within the mantle envelope of Deines (1989), and all lie within the primary igneous carbonatite field (Taylor et al., 1967) (Fig. 15). Many samples of primary BD zone dolomite (red in CL, Fig. 7A) also lie in the igneous carbonatite field (Fig. 15). In contrast, later BD zone groundmass dolomite, and all samples from the B, A and MHREO zones have heavier isotopic compositions, which may be explained by high temperature Rayleigh fractionation in the presence of a C-bearing fluid (Demény et al., 1998; Ray and Ramesh, 2000; Trofanenko et al., 2016; Liu et al., 2020). We interpret these data to indicate that the Stage 1 Rim and BD zone carbonatites crystallized under magmatic conditions. Stage 2 carbonatites were then emplaced, and exsolved a H<sub>2</sub>O-CO<sub>2</sub> fluid that equilibrated with the B, A and MHREO zone carbonate minerals as they crystallized. Exsolution of this fluid altered the BD zone carbonatite, depositing the later generation of a more Fe-rich groundmass dolomite (Fig. 6A-C). The coupled positive shift in  $\delta^{13}$ C and  $\delta^{18}$ O towards the center of the deposit could alternatively be attributed to infiltration of seawater (e.g. Demény and Ahijado, 1996), assimilation of crustal sedimentary rocks (Demény et al., 1998) or interaction with a fluid that had equilibrated with sedimentary rocks (e.g. Santos and Clayton, 1995), such as fluids produced during metamorphism. These interpretations are

- 1 precluded by the preservation of igneous isotopic compositions in the voluminous and outermost
- 2 zones of the Eldor carbonatite complex.
  - Postmagmatic Processes

Textural data and mineral compositions indicate that all Ashram zones exhibit variable effects of postmagmatic processes including recrystallization, deformation, metamorphism, and hydrothermal alteration. Indeed, carbonate minerals have a strong tendency to recrystallize, especially in the presence of fluid (Chakhmouradian et al., 2016a). Mosaic-textured Ashram carbonates (Fig. 7A,C) are likely recrystallized under low-strain conditions in the presence of a C-bearing fluid, as evidenced by their C,O isotopic compositions (Fig. 15). Recrystallized carbonates record changes in local fluid chemistry, and individual samples show variable changes in Ba, Zn, and Al contents. We suggest that at least some of the Zn for late sphalerite, and Ba (± Al) for late Ba-minerals (barite, magbasite) were supplied to the fluid by recrystallization of carbonate minerals.

It is impossible to resolve recrystallized textures due to cooling from those produced by Hudsonian deformation, which undoubtedly affected the carbonatite complex and is best manifested as localized shearing ("schlieren carbonatites" of Mitchell and Smith, 2017). The widespread preservation of vugs with complex internal textures (Fig. 6D, Fig. 7F) attests to the localized and limited extent of deformation in Ashram rocks. The origin of brittle textures exemplified by the BD (Fig. 6A-C) and MHREO (Fig. 6D-F) zone carbonates is also difficult to interpret as they may be produced by magmatic-hydrothermal processes alone, or represent deformation overprinted on primary textures. The flattened section of the breccia unit is an excellent example of such overprinting. Three-dimensional modelling of the flattened side of the breccia indicates that it has the same strike (315°) as regional thrust faults in the New Quebec Orogen (Fig. 1). We propose that the flattened part of the breccia, largely in contact with silicate wall-rocks, resulted from the concentration of regional stress in a zone of competency contrast (e.g., Ramsay, 1980). Concentrated deformation at the contacts between carbonatite and silicate rocks has been described elsewhere (e.g., Attoh et al., 2007; Casquet et al., 2008). We therefore interpret this flattened section to represent a fault breccia overprinted on an intrusive breccia.

The presence of both mineralized and unmineralized carbonatite fragments from the BD zone, the presence of mineralized veins crosscutting the matrix of the breccia, micro-faulted clasts and local ductile deformation are all evidence for reactivation along this structure and suggest that it was active from pre- to post-mineralization.

The effects of regional greenschist facies metamorphism appear to be limited. Though chlorite is present in trace amounts in all units, it predominantly occurs on fracture surfaces and abundant fresh phlogopite is present as a primary phase in the Rim calcite carbonatites, in veins in the Ashram carbonatites, and in fenites. Furthermore, magmatic C,O isotope compositions are preserved in the outermost units (Rim and BD zone) of the complex, precluding deposit-scale isotopic resetting in carbonate minerals.

There is abundant textural evidence of intense and pervasive hydrothermal overprinting in the Ashram carbonatites. The occurrence of the REE minerals monazite, xenotime and bastnäsite in veins and vugs is consistent with their precipitation from a hydrothermal fluid (Fig. 9). Monazite-(Ce) and monazite-(Nd) were the earliest REE minerals to form, followed by xenotime-(Y) and bastnasite-(Ce). The textural relationships among the carbonate minerals are complex and suggest that there were multiple alteration events. Indeed, all the major rockforming minerals at Ashram exhibit hydrothermal textures, namely secondary carbonate vug infill, veins of apatite or fluorite, and multiple generations of both minerals.

Some apatite generations can be related to one another by hydrothermal alteration. Primary BD zone apatite is compositionally indistinguishable from primary Rim apatite (Fig. 12). The BD-s apatite is interpreted to have formed by dissolution-reprecipitation of BD-p apatite, based on the observation that BD-s apatite mantles BD-p apatite, and there is a sharp boundary between the two phases (see Putnis, 2009, on textural criteria for dissolution-reprecipitation). The Rim1-p, Rim1-s and A-p, A-s apatite types can be related to one another in the same way. The coupled dissolution-reprecipitation of apatite in the presence of an aqueous fluid has been well-documented in experiments (Harlov et al., 2005) and natural samples (Harlov et al., 2002a; Putnis, 2002; Taghipour et al., 2015), including REE-mineralized carbonatites (Broom-Fendley et al., 2016; Deng et al., 2017). In the BD zone, this process did not significantly affect the absolute abundances of the REE, though their distribution changed. In the replacement reactions, the

secondary apatite (Rim1-s, BD-s, A-s) is depleted in La and Ce and enriched in Nd to Lu (Table 5), relative to the primary apatite (BD-p, A-p), indicating that the REE were mobile during this replacement. A similar HREE enrichment in secondary apatite, interpreted to have formed by the same process, has been described for the Songwe Hill carbonatite (Broom-Fendley et al., 2016).

The presence of primary apatite in the A zone that is distinct in composition from primary apatite of the Rim and BD zone also supports the case for the B and A zones representing a second pulse of magma separate from that which crystallized the outermost units of the complex. The rare B-type apatite has not been observed in contact with any other generation of apatite and, as such, its origin is unclear. It is intimately intergrown with fluorite, and has the same fine-grained, recrystallized texture as secondary Rim, BD and A zone apatite, suggesting a hydrothermal origin. Moreover, all B type apatite display Y/Y\* and Eu/Eu\* ratios well outside the ranges of igneous apatite proposed by Chakhmouradian et al. (2017) (Fig. 12).

The B type apatite may have been produced from A-p apatite, an unidentified primary apatite, or may have crystallized directly from solution. The last scenario is least likely, given the very low mobility of P in hydrothermal fluids (Poitrasson et al., 2004; Cetiner et al., 2005; Louvel et al., 2015). Both B and A-s type apatite are enriched in Sr relative to A-p apatite (Fig. 12A). This, at least partly, is an artefact of the nature of the primary apatite from which they formed, as Sr-enrichment in later generations of magmatic apatite has been observed in other carbonatites (Hogarth, 1989; Chakhmouradian et al., 2017). The enrichment in Sr in secondary apatite at Ashram may also be amplified by the Sr content of mediating fluids, possibly supplied by the dissolution of carbonate, as some generations of dolomite are depleted in Sr relative to their precursors (Table 3, Fig. 11A).

Fault Breccia, Fluid Flow and Fenitization

An acidic solution is likely required to dissolve apatite and efficiently transport the REE (Migdisov and Williams-Jones, 2014; Gysi and Williams-Jones, 2015), though it would be neutralized on contact with a carbonatite host rock, thereby limiting its efficacy in carbonatites. If, however, the solution was channelled into a limited number of pathways, the wall-rock would become progressively less reactive with successive pulses of fluid, 'armoring' the walls, eventually

inhibiting its neutralization and facilitating the continued transport of the REE. At Ashram, one such pathway could be the polymictic breccia, which surrounds and undercuts the deposit. This unit has high permeability and would have been a low-pressure zone, enabling the movement of fluid. The fault plane largely underlies the mineralized zones, and the deposit-scale zonation in REE appears to be centred on this structure (Fig. 4). Moreover, this unit contains the highest proportions of SiO<sub>2</sub>, Al<sub>2</sub>O<sub>3</sub>, Na<sub>2</sub>O, and K<sub>2</sub>O of all the Ashram units (Table 2). This and the abundance of phlogopite veinlets support the hypothesis that the fault breccia was a major pathway for fenitizing fluids. It is also noteworthy in this regard that breccias in carbonatite complexes have commonly undergone K-metasomatism (Le Bas, 2008; Elliott et al., 2018).

Building on the above discussion, we propose that the polymictic breccia was the principal conduit for the mineralizing fluids. To evaluate the efficacy of armoring in carbonatite, we constructed a thermodynamic model in which an acidic (pH= 3) 10 wt % NaCl, 5 wt % KCl, F-bearing and silica-undersaturated H<sub>2</sub>O-CO<sub>2</sub> solution at 400°C interacts with an apatite-phlogopite-siderite-bearing dolomitic carbonatite at constant pressure (500 bars). The model fluid has a molar CO<sub>2</sub>:H<sub>2</sub>O ratio of 0.41:1, and a Na:K ratio of 2, chosen to approximate the composition of carbonatitic fluids analysed by Bühn and Rankin (1999). The total salinity represents the median salinity reported in the literature for carbonatitic fluids (e.g., Smith and Henderson, 2000; Dowman et al., 2017). A trace of silica was included in the fluid to allow for precipitation of quartz and to match the presence of quartz in veins and vugs in the breccia (and the MHREO zone). The rock composition was a more dolomitic version of the average breccia composition, comprising 73% dolomite, 10% siderite, 10% phlogopite and 7% apatite, chosen to represent the breccia composition before armoring produced its current composition. Results of the model are illustrated in Fig. 17.

In our model, quartz and fluorite are deposited by the fluid, and dolomite, siderite, phlogopite and apatite are variably dissolved and re-precipitated. During the initial pulse of fluid, the pH increased by almost 3 units (3 to ~ 5.5) upon interaction with the host rock as a result of the dissolution of dolomite (Fig. 17A). This coincided with the deposition of fluorite and minor quartz. By the fifth pulse, the fluid had cooled to 350°C before its pH rose above 5. This was accompanied by further deposition of fluorite and quartz, and more significant reworking of

phlogopite, dolomite and siderite (Fig. 17B). By the tenth pulse, the fluid had cooled by another 60°C, to 290°C, before it reached pH 5, and there was abundant deposition of fluorite and quartz (Fig. 17C). Although highly simplified, this model illustrates that even in carbonatite host rocks, 'armoring' of a structure is possible through the deposition of less reactive minerals such as fluorite and quartz by successive pulses of fluid. As a result, the pH is progressively less buffered by the rock, allowing the fluid to remain acidic and capable of transporting REE.

It is unclear whether the fenitizing fluids preceded REE mineralization or were the mineralizing fluids. Depending on the locality, fenitization has been shown to predate REE-bearing fluids (e.g., Le Bas, 2008; Dowman et al., 2017) or act as the medium of mineralization (e.g., Druppel et al., 2004; Deymar et al., 2018; Elliott et al., 2018, and references therein). At Ashram, it is likely that K-metasomatism preceded REE mineralization, because a strong spatial association between phlogopite and the REE-minerals is not observed and fenitized wall rock (phlogopitite and arfvedsonite-albitite) xenoliths are unmineralized (Fig. 4). We propose instead that K-metasomatic fluids percolated through the breccia first, depositing phlogopite, thereby altering and reducing the reactivity of the conduit for the later, REE-bearing acidic fluids.

Fluid Buffering and Deposit-Scale REE Distribution

The bulk of REE-transport in F-bearing systems is thought to be achieved by REE-Cl complexes due to the pH dependence of the free fluoride activity, where the weak acid HF only dissociates to significant concentrations of free F⁻ at near-neutral or alkaline pH (Migdisov and Williams-Jones, 2014). The stability of REE-Cl complexes in aqueous fluids decreases with increasing atomic number, and the difference in their stability increases with increasing temperature, so that at ≥ 250°C, La-Cl complexes are 1.5 orders of magnitude more stable than Lu-Cl complexes (Migdisov et al., 2009). In turn, the LREE are more soluble, and therefore more mobile in aqueous solutions than the HREE, provided that the dominant ligand is chloride, something that is likely given the high salinity of carbonatite-derived fluids (e.g. Smith and Henderson, 2000; Dowman et al., 2017). Hydrothermal fluids derived from a carbonatite are expected to be strongly enriched in LREE (LREE >> HREE) (Bühn and Rankin, 1999). Accordingly, if an acidic fluid with LREE>>HREE interacts with a rock having low pH buffering capacity, it will precipitate only the most insoluble REE,

2

3

4

5

6

7

8

9

10

11

12

13

14

15

16

17

18

19

20

21

22

23

24

25

26

27

resulting in a HREE-rich rock with a low total REE concentration (Williams-Jones et al., 2015). Conversely, interaction of the same fluid with a strong buffer will result in precipitation of all the dissolved REE, producing a LREE-rich rock with a high total REE content (Migdisov and Williams-Jones, 2016). The relative pH buffering capacity of different carbonate minerals can be evaluated on the basis of their crystal lattice energy. Siderite has a lattice energy of -3206 kJ/mol, compared to -3164 and -2920 kJ/mol for dolomite and calcite, respectively (Mandell and Rock, 1998). Therefore, stronger bonds are formed between CO<sub>3</sub><sup>2-</sup> and Fe<sup>2+</sup> than between CO<sub>3</sub><sup>2-</sup> and Mg<sup>2+</sup> or Ca<sup>2+</sup>. Thus, the relative buffering capacity of the carbonate minerals is siderite < ferroan dolomite < dolomite < calcite. We propose that the differing buffering capacity of the carbonate minerals contributed to the deposit-scale zonation of MHREE/TREE at Ashram, and support this proposal with the observation that the LREE proportions of the monazite (and bastnäsite) increase with decreasing Fe content of the host carbonate minerals (Fig. 14A). Further support for this hypothesis is provided by the observation that monazite-(Nd) occurs exclusively in association with siderite, and xenotime-(Y) occurs predominantly in the siderite-hosted MHREO zone. The deposit-scale distribution of different REE-phosphate compositions and whole-rock TREO grade is thus consistent with interaction of a REE-bearing, acidic hydrothermal fluid with host rocks of variable pH buffering capacity. In the siderite host rocks, the overall grade is low, but the proportion of MHREE/TREE is relatively high, whereas the dolomite rocks are host to higher grade LREE-rich mineralization. It is noteworthy that the breccia has a TREO content and MHREE/TREE ratio (Table 2) similar to those of the MHREO zone, consistent with our model in which this zone is the conduit for the mineralizing fluids. These fluids were poorly buffered in the phlogopitefluorite-quartz-armoured pathway, resulting in a rock with a low REE grade, but a relatively high MHREE/TREE ratio. The REE composition of groundmass dolomite from the breccia supports this interpretation. Breccia dolomite displays the largest departures from igneous Y/Ho ratios (Fig. 11B), the lowest (La/Yb)<sub>CN</sub> and is the most REE-poor dolomite in the complex (Fig. 11D), consistent with flushing of LREE out of this lithology.

- 28 Monazite Mineralizing Mechanisms and Deposit-Scale Trends
- 29 Textural relationships between monazite-(Ce) and apatite and the large-scale spatial separation

of the two minerals suggest that monazite-(Ce) was deposited at the expense of apatite, via
Reaction 1:

3

4 
$$Ca_5(PO_4)_3F + 3F^- + 3REE^{3+} + CaMg(CO_3)_2 = 2CaF_2 + CaMg(CO_3)_2 + 3REEPO_4 + 3Ca^{2+}$$
 (1)  
5 apatite dol 1 fluorite dol 2 monazite

6 7

8

9

10

11

12

13

14

15

16

17

18

19

20

21

22

23

24

25

26

27

28

29

Crystallization of monazite by dissolution-reprecipitation of apatite has been documented over a wide range of pressure and temperature in experimental run products and natural samples (Smith et al., 1999; Harlov et al., 2002b; Harlov and Förster, 2003), from near-surface (Boudreau and McCallum 1990) to granulite-facies metamorphic conditions (Harlov et al., 2003). Moreover, this replacement has been reported for several carbonatites (Le Bas et al., 2004; Ani et al., 2013; Woodard and Hetherington, 2014; Decrée et al., 2016). Whether monazite nucleates during dissolution of apatite depends on the availability of the REE, which may be supplied by the fluid or the apatite (Harlov, 2015). At Ashram, the REE for monazite deposition must have been supplied by the fluid. Phosphate, however, is largely immobile in hydrothermal systems. Assuming that all the P is conserved during alteration of apatite to monazite, the amount of REE in apatite would be insufficient by one to two orders of magnitude, to produce the observed whole-rock REE grades. For example, the median P<sub>2</sub>O<sub>5</sub> content of the A zone is 1.04 wt %. If all the P in monazite was originally contained in apatite, which contains, on average, 0.8 wt % TREE, the conversion of apatite to monazite with the REE supplied by apatite, would result in a rock with a grade of only ~ 0.8 wt % TREE, more than an order of magnitude lower than the median wholerock TREE of 1.67 wt %.

Evidence for the replacement of apatite by monazite is provided by the observed mineral assemblages and paragenesis. Reaction (1) would release Ca<sup>2+</sup> and F<sup>-</sup> to form fluorite, and, if this reaction were to go to completion such that all the apatite was consumed, the resulting mineral assemblage would be monazite + fluorite + dolomite, consistent with the near absence of apatite in the monazite-dominated B, A and MHREO zones, and the common occurrence of fluorite in close spatial association with monazite (Fig. 9B). It is also consistent with the observations that fluorite is invariably later than apatite (Fig. 8E), late dolomite vug-infill in monazite-bearing zones

is widespread, and that the rare apatite in these zones is intergrown with fluorite (Fig. 8B,D,E). The B, A, and MHREO zones represent near-complete replacement of apatite by monazite whereas the apatite-rich BD zone represents only partial replacement of apatite by monazite.

1

2

3

4

5

6

7

8

9

10

11

12

13

14

15

16

17

18

19

20

21

22

23

24

25

26

27

28

29

The inverse relationship between La and Th in the monazite (Fig. 14A) is partly a crystal chemical effect. Incorporation of thorium in monazite occurs at the expense of the REE and requires a coupled substitution with Si (huttonite-type, Ni et al., 1995) or Ca (Förster 1998) to maintain charge balance. Maps of the distribution of La and Th in some monazite crystals show that a low-Th variety of monazite replaced a high-Th variety, indicating that the evolution of monazite composition was marked by a depletion in Th and an enrichment in La (Fig. 10C-F). With increasing distance from the fault, monazite became increasingly enriched in La and depleted in Th. The observed compositional trends are thus both spatial and temporal and, as such, can also be explained by the cooling of a REE-bearing fluid, consistent with observations from both nature (Schandl and Gorton, 2004) and experiments (Harlov et al., 2003, 2005; Migdisov et al., 2019) that the Th content of monazite decreases with decreasing temperature. Monazite-(Nd) and -(Ce), which deposited proximal to the fault (MHREO zone), contain the highest proportion of Th (2-5 wt% Th) of all the monazite analysed in the Ashram deposit, providing further evidence that the breccia was the conduit for the mineralizing fluid which cooled as it moved away, depositing monazite with lower Th content (e.g., B zone monazite-(Ce), < 1 wt % Th). The spatial and temporal trend in the La content of the monazite is also consistent with this cooling model. As mentioned above, La is more soluble than Lu and can remain in solution and be mobilized furthest of all the REE down a gradient of decreasing temperature (Williams-Jones et al., 2012). At Ashram, monazite-(Nd) was deposited mainly in the hanging wall proximal to the fault breccia. With increasing distance from the breccia, and therefore lower temperature, monazite-(Ce) that was progressively enriched in La, was deposited due to the higher stability of the LREE-Cl complexes compared to the HREE complexes. In summary, the observed deposit-scale variation in monazite composition through the B, A, and MHREO zones, was the cumulative product of hydrothermal fractionation of the REE by the cooling of a REE-bearing fluid as it exited the fault breccia and percolated through rocks of variable pH buffering capacity. The composition of the BD zone monazite is also explained by these processes, but lies off the trend for the A and B zones because

monazite in this zone crystallized from a different precursor magmatic apatite (Stage 1 carbonatite) than the primary apatite that crystallized during emplacement of the Stage 2 carbonatites that formed the Ashram intrusion and was subsequently altered to B, A and MHREO zone monazite. This deposit-scale zonation in LREE/HREE, centered in and around the fluid conduit and its control by the variable pH buffering capacity of the host rocks and differential stability of LREE and HREE chloride complexes, is analogous to what has been observed for the Ranger uranium deposit, Australia (Fisher et al., 2013), and proposed to explain the HREE/LREE ratio at Lofdal, Namibia (Williams-Jones et al., 2015), respectively. The origin of the monazite mineralization associated with fluorite, which is the majority of the monazite at Ashram, is explained by these mechanisms, although the origin of rare intergrowths of monazite and bastnasite documented by Mitchell and Smith (2017) is ambiguous.

Bastnäsite Mineralizing Mechanisms

Textural relationships between monazite-(Ce) and bastnäsite-(Ce), taken in conjunction with the similar spatial trends in their contents of La and Th, indicate that bastnäsite-(Ce) was either deposited by the same fluid as monazite-(Ce), or developed as a replacement of monazite-(Ce). In the latter case, this replacement would have occurred dominantly through ligand exchange ( $F^-$ ,  $CO_3^{2-}$  for  $PO_4^{3-}$ ) via the following reaction:

$$3REEPO_4 + 5CaF_2 + 3H_2O + 3CO_2 \rightarrow 3REECO_3F + Ca_5(PO_4)_3F + 6HF^{\circ}$$
 (2)

We note that although bastnäsite-(Nd) was not detected in our samples, Mitchell and Smith (2017) report its occurrence in the MHREO zone and we suggest that it formed from monazite-(Nd). The replacement of monazite by bastnäsite *via* ligand exchange has been documented in a number of geological settings (e.g., Watson and Snyman, 1975; Smith et al., 1999), including REE-mineralized carbonatites such as Phalaborwa (Giebel et al., 2017).

In the B, A, and MHREO zones where monazite is the dominant REE mineral, there was minor replacement of monazite by bastnäsite, whereas in the BD zone, bastnäsite is the dominant

mineral and likely originated from the replacement of monazite (there are traces of relict monazite, Fig. 9C,D). This explains the rarity of secondary apatite in the monazite-dominated B, A and MHREO zones, and the low proportion of fluorite in the bastnäsite-dominated BD zone.

Relative to monazite in the BD zone, the bastnäsite is enriched in La and Ce, contains an equal proportion of Pr, and is depleted in REE heavier than Pr, except for Eu (Fig. 16). Relative to primary BD-p apatite, secondary BD-s apatite is depleted in La and Ce, contains an equal proportion of Pr, and is enriched in REE heavier than Pr. Qualitatively, the REE lost from monazite during its alteration to bastnäsite were gained during the alteration of primary to secondary apatite, and *vice versa*. This suggests that at this stage, the fluid was not REE-bearing, and instead simply redistributed the elements among the various phases that were concurrently altered.

Differences in the availability of CO<sub>3</sub><sup>2-</sup> explains why there was total replacement of monazite-(Ce) by bastnäsite-(Ce) in the BD zone, but only partial replacement elsewhere. As discussed above, siderite and ferroan dolomite, which are the dominant carbonates of the interior zones, are insoluble in comparison to dolomite of the BD zone, so, although the B, A and MHREO zones host abundant CO<sub>3</sub><sup>2-</sup>, it was locked in carbonate crystals and unavailable to react with monazite to form the REE-fluorocarbonates. Similarly, deposition of Ca-bearing REE-fluorocarbonates (parisite-(Ce) and synchysite-(Ce)) would have been limited by the availability of Ca<sup>2+</sup> in solution. Calcium was readily available in the mainly dolomitic BD zone. The relative buffering capacity of the different carbonate host rocks may also explain why alteration of apatite to monazite was incomplete in the BD zone. The acidic solution responsible for the alteration would have been most strongly buffered in the BD zone, and therefore had the least effect on apatite in these rocks.

The Xenotime Problem: Sources and Hosts of the HREE

According to our model explaining the large-scale zonation of monazite, xenotime should have precipitated first. However, as shown by the observation that it mantles monazite in vugs and veins (Fig. 9E,F), xenotime deposition post-dated the crystallization of monazite. This paragenesis is explained by the following reactions:

1 
$$Ce^{3+} + PO_4^{3-} \rightarrow CePO_4$$
 log K = 37.91 (3)

2 
$$Yb^{3+} + PO_4^{3-} \rightarrow YbPO_4$$
 log K = 37.67 (4)

The equilibrium constants, K, for these reactions were calculated for 400°C and 500 bars (Shock and Helgeson, 1988, 1997; Popa and Konings, 2006; Gysi et al., 2015), with concentrations of 1 for all reactants and products. The values of these constants indicate that precipitation of monazite is slightly favoured over the precipitation of xenotime. However, carbonatite-derived fluids are expected to be strongly enriched in the LREE relative to the HREE (Bühn and Rankin, 1999). The weighted median Ce/Yb value for the MHREO zone is 294 (Table 2). Assuming that this ratio is representative of the composition of the initial mineralizing fluid, the amounts of monazite and xenotime that could precipitate are evaluated by assigning a concentration of Ce<sup>3+</sup> of 294, a Yb<sup>3+</sup> concentration of 1, and a constant PO<sub>4</sub><sup>3-</sup> concentration of 1 (unitless and meant to illustrate relative abundances only). The resultant logCePO<sub>4</sub> and logYbPO<sub>4</sub> values are 40.37 and 37.67, respectively, demonstrating that the amount of monazite expected to precipitate from such a fluid exceeds that of xenotime by three orders of magnitude. Thus, monazite crystallized earlier than xenotime because the initial mineralizing fluid was too poor in HREE.

Xenotime compositions do not show deposit-scale zonation and, consequently, cooling and pH buffering of a hydrothermal fluid did not fractionate the HREE from each other. Instead, we propose an *in situ* source of the HREE for xenotime. If the HREE were sourced from the host rock, rather than the fluid (shown above), it would account for the late deposition of xenotime, as the necessary HREE would have been 'locked' in the rock and unavailable until sufficient dissolution/alteration had occurred. *In situ* deposition of xenotime could account for the deposit-scale homogeneity in composition. There are a number of possible HREE source minerals in the host rocks. One of these is huttonite, a high temperature mineral (Harlov et al., 2007), that likely crystallized as an early magmatic phase. Huttonite is isostructural with monazite, forming a solid-solution and therefore may contain considerable proportions of REE. Though it prefers the LREE, some huttonite has been documented with 'umbrella-shaped' chondrite-normalized REE distribution patterns, with apices at Gd and containing up to 4000 ppm Y (Förster et al., 2000) which could be released during fluid-mediated alteration. This could explain the low analytical

totals and variable  $P_2O_5$  and  $REE_2O_3$  contents of the Ashram huttonite, which is a feature of altered huttonite well-documented elsewhere (e.g. Berger et al., 2008; Rekha et al., 2013; Macdonald et al., 2015). As previously discussed, HREE-Cl complexes are relatively unstable, therefore the HREE are unlikely to experience significant mobilization in a chloride-dominated system. We propose that the HREE were leached from huttonite, and redeposited *in situ* or nearly *in situ*, where  $PO_4^{3-}$  was available (e.g. Reaction 2) and thus were not fractionated due to minimal transport.

In supplying HREE to xenotime, dissolution of huttonite would have also released a significant amount of Th. Indeed, the remaining huttonite grains at Ashram are strongly depleted in Th (Table 10). The xenotime structure does not readily incorporate Th<sup>4+</sup>. Monazite, however, can incorporate large proportions of Th (Boatner, 2002). In most zones, the bulk rock Th/Ce ratios are very similar to, but slightly higher than those of the corresponding average monazite, suggesting that the dissolution of huttonite also supplied the Th for monazite. Comparison of the Th/Ce ratios of the monazite and their host rocks indicates that monazite is now the primary carrier of Th in the Ashram deposit, and that most of the huttonite was dissolved (Table 2).

Other potential HREE sources include primary A zone apatite (Reaction 1) and fluorite (). Mass balance calculations demonstrate that overall, the necessary Y for the observed trace proportion of xenotime-(Y) can be accounted for by Reaction (2), in which monazite and fluorite were consumed to form bastnäsite and secondary apatite (see Appendix). Dissolution of fluorite would have provided the bulk of the HREE and monazite the phosphate for xenotime deposition (Fig. 18).

Deposit-scale homogeneity of xenotime composition and its late paragenesis preclude a direct hydrothermal source for the HREE. We propose, instead, that xenotime crystallized later than monazite because early fluids were LREE-rich, and HREE only became available following the various replacement reactions documented above, including dissolution/alteration of huttonite, carbonate and most importantly fluorite. The fluid scavenged HREE through the hydrothermal reworking of monazite and fluorite and deposited xenotime *in* situ together with bastnäsite and secondary apatite (Fig. 18).

1 Late Nb Mineralization

2 Traces of aeschynite-(Nd) occur in veins and are associated with, but later than, monazite-(Ce)

3 and xenotime-(Y), indicating late-stage mobility of Nb in the hydrothermal fluid, and recent

4 experiments show that niobium has some mobility in fluoride-bearing solutions (Timofeev et al.,

5 2015). The replacement of monazite by bastnäsite would have produced HF (Reaction 2), which,

6 depending on the temperature and pH, would have disassociated (Migdisov and Williams-Jones,

2014), making fluoride ions available for complexation with Nb, thereby enabling its mobilization.

8 We propose that aeschynite-(Nd) was deposited after the reworking of primary Nb-bearing

minerals by late, fluoride-rich fluids produced during the alteration of monazite to bastnäsite.

Another secondary Nb mineral, samarskite-(Y), which was described by Mitchell and Smith (2017)

but not identified in our samples, is also interpreted to have been deposited by these fluids.

Potential sources of Nb for aeschynite-(Nd) and samarskite-(Y), include ferrocolumbite and

niobian rutile, which occur in trace (< 1 vol %) amounts in the Ashram carbonatites (Mitchell and

14 Smith, 2017).

7

9

10

11

12

13

16

17

18

19

20

21

22

23

24

25

26

27

28

29

**15** *Genetic Model* 

We propose the following model for the genesis of the REE mineralization of the Ashram deposit (Fig. 19). The first stage of carbonatite emplacement produced the Rim and BD zones, and involved a magma with a low concentration of REE, and a high concentration of P (Fig. 19A). This was followed by the emplacement of a second carbonatite magma, represented by the B, A and MHREO zones, and characterized by high REE and low P contents (Fig. 19B). Both magmas crystallized their own distinct, primary apatite, though apatite was significantly more abundant in the Stage 1 magma. The intrusions were accompanied by faulting and brecciation caused by the regional stresses of the New Quebec Orogen. The second carbonatite magma (Stage 2) exsolved a H<sub>2</sub>O-CO<sub>2</sub> fluid and altered the BD zone, which is located within the complex at the contact between the Stage 1 and Stage 2 carbonatites (Fig. 19C). This carbonatite-derived, REE-bearing fluid utilized the fault breccia as a conduit and rose through the hanging wall. The REE were fractionated as the mineralizing fluid left the fault and interacted with rocks of variable pH buffering capacity as it cooled, evident from the occurrence of increasingly LREE-rich monazite

with increasing distance from the fault. On interaction with its host (the Stage 2 carbonatites) the

2

3

4

5

6

7

8

9

10

11

12

13

14

15

16

17

18

19

20

21

22

23

24

25

26

27

28

29

fluid altered primary apatite to an assemblage of monazite, fluorite and dolomite (Reaction 1) (Fig. 19D). In the apatite-poor B, A and MHREO zones, prolonged fluid-rock interaction resulted in nearly complete consumption of apatite, thereby providing the phosphate for monazite deposition. In the BD zone, where fluid-rock ratios were low and the pH buffering capacity and initial apatite content was high compared to the inner parts of the Ashram carbonatite, there was only partial replacement of apatite by monazite. Later, monazite and fluorite interacted with a H<sub>2</sub>O(-CO<sub>2</sub>) fluid and were replaced by bastnäsite, secondary apatite and xenotime (Fig. 19E). At this stage, the fluid was REE-barren, and simply transferred REE between the reactant and product phases. In the B, A, and MHREO zones, only a small proportion of monazite was replaced by bastnäsite due to the lack of available CO<sub>3</sub><sup>2-</sup>. Lastly, Nb was remobilized and deposited as trace aeschynite-(Nd) by late-stage, F-rich fluids produced during the alteration of monazite to bastnäsite.

The deposit-scale zonation of the mineralogy and the REE distribution, including the peculiar zone of MHREE enrichment, can be attributed to the cooling and pH buffering of a hydrothermal fluid as it travelled up and outward from a fault breccia. Upon its exit from this conduit, the REE-bearing fluid was at its highest temperature and its pH was buffered only weakly by the siderite of the MHREO zone. This resulted in the deposition of the most La-depleted, and Th-rich variety of monazite (monazite-(Nd)). Xenotime deposition was largely limited to the MHREO zone because of the close proximity of this zone to the fault, and the high fluid/rock ratio. Xenotime was deposited later than monazite because of the time necessary for the fluid to alter/dissolve the pre-existing mineral assemblage and leach the HREE. Travelling away from the fault, the fluid cooled and was progressively buffered to higher pH as it passed through dolomitic rocks with a lower Fe content, allowing it to deposit monazite with a higher proportion of La. Relative to the BD zone, the apatite-poor B, A and MHREO zones buffered the pH of the acidic mineralizing fluid less strongly, allowing apatite-monazite replacement reactions to proceed to completion, consistent with the near absence of apatite and the abundance of secondary fluorite and dolomite in these zones. In the BD zone with extremely abundant apatite, these reactions terminated well before all the apatite could be converted to monazite. This also explains the overall lower REE grade (see Table 1) of the BD zone; apatite was not sufficiently altered to

concentrate the REE to potentially economic levels. The higher pH buffering capacity of the BD zone dolomite neutralized the acidic fluid more rapidly, limiting the extent to which monazite replaced apatite. For this same reason, replacement of monazite by bastnäsite was essentially complete in the BD zone, as CO<sub>3</sub><sup>2-</sup> was readily available for reaction. The relationship between apatite, monazite and bastnäsite in the BD zone is exemplified in Fig. 9C,D. In summary, the deposit-scale zonation in mineralogy and REE distribution at Ashram was the result of REE fractionation along the fluid pathway due to cooling and variations in the pH buffering capacity of the different host rocks with which the fluid interacted. This allowed the lightest REE to travel the furthest from the breccia and produce the deposit scale separation of the light from the heavy REE, which is a striking feature of the Ashram carbonatite.

12 Conclusions

The REE mineralization at Ashram is hydrothermal in origin and was produced through a series of fluid-mediated replacement reactions. Nonetheless, magmatic processes were also important in determining the initial distribution of the REE. There were two stages of carbonatite emplacement, each geochemically distinct. Rare earth element-mobilizing H<sub>2</sub>O-CO<sub>2</sub> fluids were exsolved from the Stage 2 carbonatite magma. These fluids were acidic, REE-bearing and utilized a central fault breccia as a conduit of egress, with successive pulses armouring the pathway, preventing neutralization and allowing for the transport of a large mass of the REE. Cooling and differential pH buffering of the fluid along this conduit resulted in fractionation of the REE and the observed REE zonation at Ashram, including the MHREE-enriched zone, all centered on the fault breccia. The evolving composition of the fluid and its interaction with host rocks of variable bulk composition and pH buffering capacity resulted in a REE-phosphate-rich deposit with large-scale, antipathic separation of monazite + fluorite and bastnäsite + apatite. Ashram had a long-lived history in which the combination of magmatic zone-refinement and hydrothermal mobilization contributed to the formation of a potentially economic carbonatite-hosted REE deposit.

1 Acknowledgements

- 2 The research presented in this manuscript was supported financially by a MITACS grant to
- 3 Diversification de l'exploration minerale au Quebec (DIVEX) and a NSERC Discovery Grant to AEW-
- 4 J. Commerce Resources Corp. and Dahrouge Geological Consulting Ltd. provided access to the
- 5 site, drill core and assay data. Matthew Carter and Alex Knox with Dahrouge provided valuable
- 6 insight to deposit geology on site. We are grateful to Lang Shi for extensive help with the
- 7 microprobe analyses, and to Thi Hao Bui for help with the C-O isotope analyses. Our thanks also
- 8 go to Olga Vasyukova and Rowan Wollenberg for many helpful discussions. The manuscript was
- 9 greatly improved from the constructive comments of Associate Editor Anton Chakhmouradian
- 10 and three anonymous reviewers.

12

13

14

15 16

17

18

19 20

21

22

2324

25

26

27

28 29

30

31

32

33

34 35

36

11 References

- Ani, T.A., and Sarapaa, O., 2013, Geochemistry and mineral phases of REE in Jammi carbonatite veins and fenites, southern end of the Sokli complex, NE Finland: Geochemistry, Exploration, Environment, Analysis, v. 13, p. 217-224.
- Attoh, K., Corfu, F., and Nude, P.M., 2007, U-Pb zircon age of deformed carbonatite and alkaline rocks in the Pan-African Dahomeyide suture zone, West Africa: Precambrian Research, v. 155, p. 251-260.
- Berger, A., Gnos, E., Janots E., Fernandez, A., and Giese, J., 2008, Formation and composition of rhabdophane, bastnäsite and hydrated thorium minerals during alteration: implications for geochronology and low-temperature processes: Chemical Geology, v. 254, p. 238-248.
- Boatner, L.A., 2002, Synthesis, structure and properties of monazite, pretulite and xenotime: Reviews in Mineralogy and Geochemistry, v. 48, p. 87-121.
- Bodeving, S., Williams-Jones, A.E., and Swinden, S., 2017, Carbonate-silicate immiscibility, REE mineralising fluids, and the evolution of the Lofdal Intrusive Suite, Namibia: Lithos, v. 268-271, p. 383-398.
- Boudreau, A.E., and McCallum, I.S., 1990, Low temperature alteration of REE-rich chlorapatite from the Stillwater Complex, Montana: American Mineralogist, v. 75, p. 687-693.
- Broom-Fendley, S., Styles, M.T., Appleton, J.D., Gunn, G., and Wall, F., 2016, Evidence for dissolution-reprecipitation of apatite and preferential LREE-mobility in carbonatite-derived late-stage hydrothermal processes: American Mineralogist, v. 101, p. 596-611.
- Bühn, B., 2008, The role of the volatile phase for REE and Y fractionation in low-silica carbonate magmas: implications from natural carbonatites, Namibia: Mineralogy and Petrology, v. 92, p. 453-470.
- Bühn, B., and Rankin, A.H., 1999, Composition of natural, volatile-rich Na-Ca-REE-Sr carbonatitic fluids trapped in fluid inclusions: Geochimica et Cosmochimica Acta, v. 63, p. 3781-3797.
- 37 Bühn, B., Rankin, A.H., Schneider, J., and Dulski, P., 2002, The nature of orthomagmatic,

carbontitic fluids precipitating REE, Sr-rich fluorite: fluid inclusion evidence from the Okorusu fluorite deposit, Namibia: Chemical Geology, v. 186, p. 75-98.

- Castor, S.B., and Hedrick, J.B., 2006, Rare earth elements, in Kogel, J.E., Trivedi, N.C., Barker, J.M., eds., Industrial Minerals and Rocks, 7<sup>th</sup> ed.: Littleton, Colorado, Society for Mining, Metallurgy and Exploration, p. 769-792
- Castor, S.B., 2008, The Mountain Pass Rare-Earth Carbonatite and Associated Ultrapotassic Rocks, California: The Canadian Mineralogist, v. 46, p. 779-806.
- Casquet, C., Pankhurst, R.J., Galindo, C., Rapela, A., Fanning, C.M., Baldo, E., Dahlquist, J., Gonzalez Casado, J.M., and Colombo, F., 2008, A deformed alkaline igneous rock-carbonatite complex from the Western Sierras Pampeanas, Argentina: Evidence for late Neoproterozoic opening of the Clymene Ocean?: Precambrian Research, v. 165, p. 205-220.
- Chakhmouradian, A.R., Reguir, E.P., and Zaitsev, A.N., 2016a, Calcite and dolomite in intrusive carbonatites. I. Textural variations: Mineralogy and Petrology, v. 110, p. 333-360.
- Chakhmouradian, A.R., Reguir, E.P., Couëslan, C., and Yang, P., 2016b, Calcite and dolomite in intrusive carbonatites. II. Trace-element variations: Mineralogy and Petrology, v. 110, p. 361-377.
- Chakhmouradian, A.R., Reguir, E.P., Zaitsev, A.N., Couëslan, C., Cheng, X., Kynicky, J., Mumin, A.H., and Yang, P., 2017, Apatite in carbonatitic rocks: Compositional variation, zoning, element partitioning and petrogenetic significance: Lithos, v. 274-275, p. 188-213.
- Clark, T., and Wares, R., 2006, Lithotectonic and Metallogenic Synthesis of the New Quebec Orogen (Labrador Trough). MM 2005-01.
- Costanzo, A., Moore, K.R., Wall, F. and Freely, M., 2006, Fluid inclusions in apatite from Jacupiranga calcite carbonatites: Evidence for a fluid-stratified carbonatite magma chamber: Lithos, v. 91, p. 208-228.
- Decrée, S., Boulvais, P., Tack, L., Andre, L., and Baele, J.M., 2016, Fluorapatite in carbonatite-related phosphate deposits: The case of the Matongo carbonatie (Burundi): Mineralium Deposita, v. 51, p. 453-466.
- Deines, P., 1989, Stable isotope variations in carbonatites, in Bell, K., ed., Carbonatites, genesis and evolution: London, UK, Unwin Hyman Ltd., p. 301-359.
- Deng, M., Xu, C., Song, W., Tang, H., Liu, Y., Zhang, Q., Zhou, Y., Feng, M., and Wei, C., 2017, REE mineralization in the Bayan Obo deposit, China: Evidence from mineral paragenesis: Ore Geology Reviews, v. 91, p. 100-109.
- Demény, A., and Ahijado, A., 1996, A stable isotope study on the evolution of Canary Island carbonatites: Acta Geologica Hungarica, v. 39, p. 25-26.
- Demény, A., Ahijado, A., Casillas, R., and Vennemann, T.W., 1998, Crustal contamination and fluid/rock interaction in the carbonatites of Fuerteventura (Canary Islands, Spain): a C, O, H isotope study: Lithos, v. 44. P. 101-115.
- Deymar, S., Yazdi, M., Rezvanianzadeh, M.R., and Behzadi, M., 2018, Alkali metasomatism as a process for Ti-REE-Y-U-Th mineralization in the Saghand Anomaly 5, Central Iran: Insights from geochemical, mineralogical and stable isotope data: Ore Geology Reviews, v. 93, p. 308-336.
- Doroshkevich, A.G., Viladkar, S.G., Ripp, G.S., and Burtseva, M.V., 2009, Hydrothermal REE mineralization in the Amba Dongar Carbonatite Complex, Gujarat, India: The Canadian

1 Mineralogist, v. 47, p. 1105-1116.

- Dowman, E, 2014, Mineralisation and Fluid Processes in the Alteration Zone Around the Chilwa Island and Kangankunde Carbonatite Complexes, Malawi: Unpublished Ph.D. thesis, London, UK, Kingston University.
- Dowman, E., Wall, F., Treloar, P.J., and Rankin, A.H., 2017, Rare-earth mobility as a result of multiple phases of fluid activity in fenite around the Chilwa Island Carbonatite, Malawi: Mineralogical Magazine, v. 81, p. 1367-1395.
- Dressler, B. (1979). Region de la Fosse du Labrador (56°30′-57°15′). Ministere des Richesses naturelles, Quebec; RG 195.
- Druppel, K., Hoefs, J., and Okrusch, M., 2004, Fenitizing Processes Induced by Ferrocarbonatite Magmatism at Swartbooisdrif, NW Namibia: Journal of Petrology, v. 46, p. 377-406.
- Elliott, H.A.L., Wall, F., Chakhmouradian, A.R., Siegfried, P.R., Dahlgren, S., Weatherley, S., Finch, A.A., Marks, M.A.W., Dowman, E., and Deady, E., 2018, Fenites associated with carbonatite complexes: A review: Ore Geology Reviews, v. 93, p. 38-59.
- Flemming, R.L., 2007, Micro X-ray diffraction (μXRD): A versatile technique for characterization of Earth and planetary materials: Canadian Journal of Earth Sciences, v. 44: 1333-1346.
- Finger, F., Broska, I., Roberts, M.P., and Schermaier, A., 1998, Replacement of primary monazite by apatite-allanite-epidote coronas in an amphibolite facies granite gneiss from the eastern Alps: American Mineralogist, v. 83, p. 248-258.
- Fisher, L.A., Cleverley, J.S., Pownceby, M., and MacRae, C., 2013, 3D representation of geochemical data, the corresponding alteration and associated REE mobility at the Ranger uranium deposit, Northern Territory, Australia: Mineralium Deposita, v. 48, p. 947-966.
- Förster, H.J., 1998, The chemical composition of REE-Y-Th-U accessory minerals in peraluminous granites of the Erzgebirge-Fichtelgebirge region, Germany, Part I: the monazite-(Ce)-brabantite solid solution series: American Mineralogist, v. 83, p. 259-272.
- Förster, H.-J., Harlov, D.E., and Milke, R., 2000, Composition and Th-U-Total Pb ages of huttonite and thorite from Gillespie's Beach, South Island, New Zealand: The Canadian Mineralogist, v. 38, p. 675-684.
- Gammons, C.H., Wood, S.A., and Li, Y., 2002, Complexation of the rare earth elements with aqueous chloride at 200°C and 300°C and saturated water vapor pressure: Geochemical Society Special Publication, v. 7, p. 191-207.
- Gagnon, G., Rousseau, G., Camus, Y., and Gagne, J. (2015). Ashram Rare Earth Deposit, Preliminary Economic Assessment. NI 43-101 Technical Report, Prepared by SGS Geostat Canada for Commerce Resources, 202 p.
- Giebel, R.J., Gauert, C.D.K., Marks, M.A.W., Costin, G., and Markl, G., 2017, Multi-stage formation of REE minerals in the Palabora Carbonatite Complex, South Africa: American Mineralogist, v. 102, p. 1218-1233.
- Gomide, C.S., Brod, J.A., Vieira, L.C., Junqueira-Brod, T.C., Petrinovic, I.A., Santos, R.V., Barbosa, E.S.R., and Mancini, L.H., 2016, Stable (C, O, S) isotopes and whole-rock geochemistry of carbonatites from Alto Paranaiba Igneous Province, SE Brazil: Brazilian Journal of Geology, v. 46, p. 351-376.
- Gysi, A.P., and Williams-Jones, A.E., 2015, The thermodynamic properties of bastnäsite-(Ce)

and parisite-(Ce): Chemical Geology, v. 392, p. 87-101.

- Gysi, A.P., Williams-Jones, A.E., and Harlov, D.E., 2015, The solubility of xenotime-(Y) and other HREE phosphates (DyPO4, ErPO4 and YbPO4) in aqueous solutions from 100 to 250 degrees C and p(sat): Chemical Geology, v. 401, p. 83-95.
- Harlov, D.E., and Förster, H.J., 2003, Fluid-induced nucleation of (Y+REE)-phosphate minerals within apatite: Nature and experiment. Part II. Fluorapatite: American Mineralogist, v. 88, p. 1209-1229.
- Harlov, D.E., Andersson, U.B., Förster, H.J., Nystrom, J.O., Dulski, P., and Broman, C., 2002a, Apatite-monazite relations in the Kirrunavaara magnetite-apatite ore, northern Sweden: Chemical Geology, v. 191, p. 47-72.
- Harlov, D.E., Förster, H.J., and Nijland, T.G., 2002b, Fluid-induced nucleation of (Y + REE)-phosphate minerals within apatite: nature and experiment. Part I. Chlorapatite: American Mineralogist, v. 87, p. 245-261.
- Harlov, D.E., Forster, H.-J., and Schmidt, C., 2003, High P-T experimental metasomatism of a fluorapatite with significant britholite and fluorellestadite components: implications for LREE mobility during granulite-facies metamorphism: Mineralogical Magazine, v. 67, p. 61-72.
- Harlov D.E., Wirth R., and Förster, H.J., 2005, An experimental study of dissolution-reprecipitation in fluorapatite: fluid infiltration and the formation of monazite: Contributions to Mineralogy and Petrology, v. 150, p. 268-286.
- Harlov, D.E., Wirth, R., and Hetherington, C.J., 2007, The relative stability of monazite and huttonite at 300-900°C and 200-1000 MPa: Metasomatism and the propagation of metastable mineral phases: American Mineralogist, v. 92, p. 1652-1664.
- Harlov, D.E., 2015, Apatite: a fingerprint for metasomatic processes: Elements, vol 11, p. 171-176.
- Heinrich, E.W., 1966, The Geology of Carbonatites: Chicago, Rand McNally & Company, 555 p. Hogarth, D.D., 1989, Pyrochlore, apatite and amphibole: distinctive minerals in carbonatite, in Bell, K., ed., Carbonatites, genesis and evolution: London, UK, Unwin Hyman Ltd., p. 301-359.
- Holland, T.J.B., and Powell, R., 1998, An internally consistent thermodynamic data set for phases of petrological interest: Journal of Metamorphic Geology, v. 16, p. 309-343.
- Hornig-Kjarsgaard, I., 1998, Rare earth elements in sövitic carbonatites and their mineral phases: Journal of Petrology, v. 39, p. 2105-2121.
- Johnson, J.W., Oelkers, E.H., and Helgeson, H.C., 1992, SUPCRT92: A software package for calculating the standard molal thermodynamic properties of minerals, gases, aqueous species and reactions from 1 to 5000 bar and 0 to 1000C: Computers and Geosciences, v. 18, p. 899-947.
- Kapustin, Y.L., 1971, Mineralogy of carbonatites (English translation, 1980): New Delhi, India, Amerind Publishing Co, 259 p.
- Kestin, J., Sengers, J., and Kamgar-Parsi, B., 1984, Thermophysical properties of fluid H20: Journal of Physical and Chemical Reference Data, v. 13, p. 175-183.
- Le Bas, M.J., 1977, Magmatic and metasomatic processes, in Le Bas, M.J., ed., Carbonatite-Nephelinite Volcanism: An African Case History, New York, John Wiley & Sons, p. 263-278.
- Le Bas, M.J., 2008, Fenites associated with carbonatites: The Canadian Mineralogist, v. 46, p.

1 915-932.

- Le Bas, M.J., Ba-bttat, M.A.O., Taylor, R.N., Milton, J.A., Windley, B.F., and Evins, P.M., 2004, The carbonatite-marble dykes of Abyan Province, Yemen Republic: The mixing of mantle and crustal carbonate materials revealed by isotope and trace element analysis: Mineralogy and Petrology, v. 82, p. 105-135.
- Le Bas, M.J., and Handley, C.D., 1979, Variation in apatite composition in ijolitic and carbonatitic igneous rocks: Nature, v. 279, p. 54-56.
- Liu, S., Fan, H.-R., Groves, D.I., Yang, K.-Y., Yang, Z.-F., and Wang, Q.-W., 2020, Multiphase carbonatite-related magmatic and metasomatic processes in the genesis of the orehosting dolomite in the giant Bayan Obo REE-Nb-Fe deposit: Lithos, v. 354-355, 10.1016/j.lithos.2019.105359
- Macdonald, R., Baginski, B., Kartashov, P.M., Zozulya, D., Dzierzanowski, P., and Jokubauskas, P., 2015, Hydrothermal alteration of a chevkinite-group mineral to a bastnäsite-(Ce)-ilmenite-columbite-(Fe) assemblage: interaction with a F-, CO2-rich fluid: Mineralogy and Petrology, v. 109, p. 659-678.
- Machado, N., Clark, T., David, J., and Goulet, N., 1997, U-Pb ages for magmatism and deformation in the New Quebec Orogen: Canadian Journal of Earth Science, v. 34, p. 716-723.
- Mandell, G. K., and Rock, P.A., 1998, Lattice energies of calcite-structure metal carbonates II. Results for CaCO<sub>3</sub>, CdCO<sub>3</sub>, FeCO<sub>3</sub>, MgCO<sub>3</sub> and MnCO<sub>3</sub>: Journal of Physical Chemistry of Solids, v. 5, p. 703-712.
- Mariano, A.N., 1989, Nature of economic mineralization in carbonatites and related rocks, in Bell, K., ed., Carbonatites: Genesis and Evolution, Winchester, Massachusetts, Unwin Hyman Inc., p. 149-176.
- Marshall, W.L. and Franck, E.U., 1981, Ion Product of Water Substance, 0-1000C, 1-10,000 Bars, New International Formulation and Its Background: Journal of Physical and Chemical Reference Data, v. 10, p. 295-304.
- McDonough, W.F., Sun, S.-S., 1995, The composition of the Earth: Chemical Geology, v. 120, p. 223-253.
- Migdisov, A.A., and Williams-Jones, A.E., 2008, A spectrophotometric study of Nd (III), Sm (III) and Er (III) complexation in sulfate-bearing solutions at elevated temperatures: Geochimica Cosmochimica Acta, v. 72, p. 5291-5303.
- Migdisov, A.A. and Williams-Jones, A.E., 2014, Hydrothermal transport and deposition of the rare earth elements by fluorine-bearing aqueous liquids: Mineralium Deposita, v. 49, p. 987-997.
- Migdisov, A.A., Williams-Jones, A.E., and Wagner, T., 2009, An experimental study of the solubility and speciation of the Rare Earth Elements (III) in fluoride- and chloride-bearing aqueous solutions at temperatures up to 300°C: Geochimica et Cosmochimica Acta, v. 73, p. 7087-7109.
- Migdisov, A.A., Williams-Jones, A.E., Brugger, J., and Caporuscio, F.A., 2016, Hydrothermal transport, deposition and fractionation of the REE: Experimental data and thermodynamic calculations: Chemical Geology, v. 439, p. 13-42.
- Migdisov, A.A., Guo, X., Nisbet, H., Xu, H., and Williams-Jones, A.E., 2019, Fractionation of REE, U and Th in natural ore-forming hydrothermal systems: Thermodynamic modeling:

1 Journal of Chemical Thermodynamics, v. 128, p. 305-319.

- Mitchell, R.H., and Smith, D.L., 2017, Geology and mineralogy of the Ashram Zone carbonatite, Eldor Complex, Quebec: Ore Geology Reviews, v. 86, p. 784-806.
- Moore, M., Chakhmouradian, A.R., Mariano, A.N., and Sidhu, R., 2015, Evolution of rare-earth mineralization in the Bear Lodge carbonatite, Wyoming: Mineralogical and isotopic evidence: Ore Geology Reviews, v. 64, p. 499-521.
- Mott, A.V., Bird, D.K., Grove, M., Rose, N., Bernstein, S., Mackay, H. and Krebs, J., 2013, Karrat Isfjord: A newly discovered Paleoproterozoic carbonatite-sourced REE deposit, Central West Greenland: Economic Geology, v. 108, p. 1471-1488.
- Nadeau, O., Cayer, A., Pelletier, M., Stevenson, R., and Jébrak, M., 2015, The Paleoproterozoic Montviel carbonatite-hosted REE-Nb deposit, Abitibi, Canada: Geology, mineralogy, geochemistry and genesis: Ore Geology Reviews, v. 67, p. 314-335.
- Ni, Y., Hughes, J.M., and Mariano, A.N., 1995, Crystal chemistry of the monazite and xenotime structures: American Mineralogist, v. 80, p. 21-26.
- Oelkers, E.H., and Poitrasson, F., 2002, An experimental study of the dissolution stoichiometry and rates of a natural monazite as a function of temperature from 50 to 230°C and pH from 1.5 to 10: Chemical Geology, v. 191, p. 73-87.
- Olson, J.C., Shawe, D.R., Pray, L.C., and Sharp, W.N., 1954, Rare-earth mineral deposit of the Mountain Pass district, San Bernardino County, California, U.S. Geological Survey Professional Paper 261, p. 1-75.
- Paton, C., Hellstrom, J., Paul, B., Woodhead, J., and Hergt, J., 2011, Iolite: Freeware for the visualisation and processing of mass spectrometric data: Journal of Analytical Atomic Spectrometry, v. 26, p. 2508.
- Pell, J., 1996, Mineral deposits associated with carbonatites and related alkaline igneous rocks, in Mitchell, R.R., ed., Undersaturated Alkaline Rocks: Mineralogy, Petrogenesis, and Economic Potential, Mineralogical Association of Canada, Short Course Series, Winnipeg, p. 271-310.
- Poitrasson, F., Oelkers, E., Schott, J., and Montel, J.M., 2004, Experimental determination of synthetic NdPO<sub>4</sub> monazite end-member solubility in water from 21 degrees C to 300 degrees C: implications for rare earth element mobility in crustal fluids: Geochimica et Cosmochimica Acta, v. 68, p. 2207-2221.
- Popa, K., and Konings, R.J.M., 2006, High-temperature heat capacities of EuPO4 and SmPO4 synthetic monazites: Thermochimica Acta, v. 445, p. 49-52.
- Putnis, A., 2002, Mineral replacement reactions: from macroscopic observations to microscopic mechanisms: Mineralogical Magazine, v. 66, p. 689-708.
- Putnis, A., 2009, Mineral replacement reactions: Reviews in Mineralogy and Geochemistry, v. 70, p. 87-124.
- Ramsay, J.G., 1980, Shear zone geometry a review: Journal of Structural Geology, v. 2, p. 83-99.
- Ray, J.S., and Ramesh, R., 2000, Rayleigh fractionation of stable isotopes from a multicomponent source: Geochimica et Cosmochimica Acta, v. 64, p. 299-306.
- Rekha, S., Bhattacharya, A., and Viswanath, T.A., 2013, Microporosity linked fluid focusing and monazite instability in greenschist facies para-conglomerates, western India: Geochimica et Cosmochimica Acta, v. 105, p. 187-205.

Robie, R.A., and Hemingway, B.S., 1995, Thermodynamic properties of minerals and related substances at 298.15 K and 1 Bar (105 Pascals) pressures and at higher temperatures. US Geological Survey Bulletin, 2131, 461 p.

- Ruberti, E., Enrich, G.E.R., and Gomes, C.B., 2008, Hydrothermal REE fluorocarbonate mineralization at Barra Do Itapirapua, a multiple stockwork carbonatite, Southern Brazil: The Canadian Mineralogist, v. 46, p. 901-914.
- Santos, R.V., and Clayton, R.N., 1995, Variations of oxygen and carbon isotopes in carbonatites: A study of Brazilian alkaline complexes: Geochimica et Cosmochimica Acta, v. 59, p. 1339-1352.
- Schandl, E.S., and Gorton, M.P., 2004, A textural and geochemical guide to the identification of hydrothermal monazite: Criteria for selection of samples for dating epigenetic hydrothermal ore deposits: Economic Geology, v. 99, p. 1027-1035.
- Schmidt, P. T., 2013, High-field-strength element distribution of the Eldor carbonatite complex, Canada: Unpublished M.Sc. thesis, Tübingen, Germany, The University of Tübingen, 173 p.
- Shock, E.L., Sassani, D.C., Willis, M., and Sverjensky, D.A., 1997, Inorganic species in geologic fluids: Correlations among standard molal thermodynamic properties of aqueous ions and hydroxide complexes: Geochimica et Cosmochimica Acta, v. 61, p. 907-950.
- Shock, E.L., and Helgeson, H.C., 1988, Calculation of the thermodynamic and transport properties of aqueous species at high pressures and temperatures: Correlation algorithms for ionic species and equation of state preditions to 5 kb and 1000°C: Geochimica et Cosmochimica Acta, v. 52, p. 2009-2036.
- Shvarov, Y., and Bastrakov, E., 1999, HCh: a software package for geochemical equilibrium modelling user's guide, Australian Geological Survey Organisation, Record 1999/25, 61 p.
- Siegel, K., Williams-Jones, A.E., and van Hinsberg, V.J., 2017, The amphiboles of the REE-rich A-type peralkaline Strange Lake pluton fingerprints of magma evolution: Lithos, v. 288-289, p. 156-174
- Smith, M.P., and Henderson, P., 2000, Preliminary fluid inclusion constraints on fluid evolution in the Bayan Obo Fe-REE-Nb deposit, Inner Mongolia, China: Economic Geology, v. 95, p. 1371-1388.
- Smith, M.P., Henderson, P., Zhang, P., 1999, Reaction relationships in the Bayan Obo Fe-REE-Nb deposit Inner Mongolia, China: implications for the relative stability of rare-earth element phosphates and fluorocarbonates: Contributions to Mineralogy and Petrology, v. 134, p. 294-310.
- Smith, M.P., Campbell, L.S. and Kynicky, J., 2015, A review of the genesis of the world class Bayan Obo Fe-REE-Nb deposits, Inner Mongolia, China: Multistage processes and outstanding questions: Ore Geology Reviews, v. 64, p. 459-476.
- Sverjensky, D.A., Shock, E.L., and Helgeson, H.C., 1997, Prediction of the thermodynamic properties of aqueous metal complexes to 1000C and 5kb: Geochimica et Cosmochimica Acta, v. 61, p. 1359-1412.
- Swinden, S., and Hall, M., 2012, Mkango Resources Ltd: NI 43-101 technical report and mineral resource estimate for the Songwe Hill rare earth element REE project, Phalombe District, Republic of Malawi, MSA Group Technical report.

Taghipour, S., Kananian, A., Harlov, D., and Oberhansli, R., 2015, Kiruna-type Iron oxide-apatite deposits, Bafq District, Central Iran: Fluid-aided genesis of fluorapatite-monazite-xenotime assemblages: The Canadian Mineralogist, v. 53, p. 479-496.

- Tagirov, B.R., Zotov, A., Akinfiev, N., 1997, Experimental study of dissociation of HCl from 350 to 500C and from 500 to 2500 bars: thermodynamic properties of HCl (aq): Geochimica et Cosmochimica Acta, v. 61, p. 4267-4280.
- Taylor, H.P., Frechen, J., and Degens, E.T., 1967, Oxygen and carbon isotope studies of carbonatites from the Laacher See District, West Germany and the Alno District, Sweden: Geochimica et Cosmochimica Acta, v 31, p. 407-430.
- Timofeev, A., Migdisov, A.A., and Williams-Jones, A.E., 2015, An experimental study of the solubility and speciation of niobium in fluoride-bearing aqueous solutions at elevated temperature: Geochimica et Cosmochimica Acta, v. 158, p. 103-111.
- Trofanenko, J., Williams-Jones, A.E., Simandl, G.J., and Migdisov, A.A., 2016, The nature and origin of the REE mineralization in the Wicheeda carbonatite, British Columbia, Canada: Economic Geology, v. 111, p 199-223.
- Watson, M.D., and Snyman, C.P., 1975, The geology and the mineralogy of the fluorite deposits at the Buffalo Fluorspar mine on Buffelsfontein, 346KR, Naboomspruit District: Transactions of the Geological Society of South Africa, v. 78, p. 137-151.
- Williams-Jones, A.E., Wollenberg, R., and Bodeving, S., 2015, Hydrothermal fractionation of the rare earth elements and the genesis of the Lofdal REE deposit, Namibia [ext. abs.] Symposium on Strategic and Critical Materials Proceedings, November 13-14, 2015, Victoria, British Columbia, British Columbia Ministry of Energy and Mines, British Columbia Geological Survey Paper 2015-3, pp. 125-130.
- Woodard, J., and Hetherington, C.J., 2014, Carbonatite in a post-collisional tectonic setting: Geochronology and emplacement conditions at Naantali, SW Finland: Precambrian Research, v. 240, p. 94-107.
- Xie, Y., Hou, Z., Yin, S., Dominy, S.C., Xu, J., Tian, S., and Xu, W., 2009, Continuous carbonatitic melt-fluid exsolution of a REE-mineralisation system: Evidence from Inclusion in the Maoniuping REE Deposit, Western Sichuan, China: Ore Geology Reviews, v. 36, p. 90-105.
- Xie, Y., Li, Y., Hou, Z., Cooke, D.R., Danyushevsky, L., Dominy, S.C., and Yin, S., 2015, A model for carbonatite hosted REE mineralisation the Mianning-Dechang REE belt, Western Sichuan Province, China: Ore Geology Reviews, v. 70, p. 595-612.

1 Figures

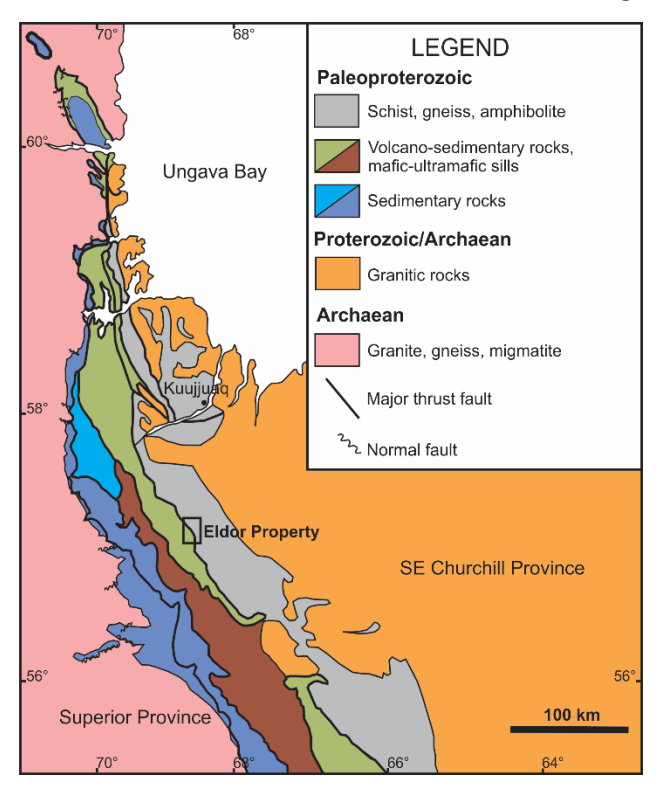


Fig. 1: A regional geological map, showing the location of the Eldor carbonatite complex in the New Quebec Orogen (after Clark and Wares, 2006).

Fig. 2 A) A simplified geological map of the Eldor Carbonatite Complex at the 100 m level, based on information from drill core. B) A simplified cross-section of the X-X' transect in A)

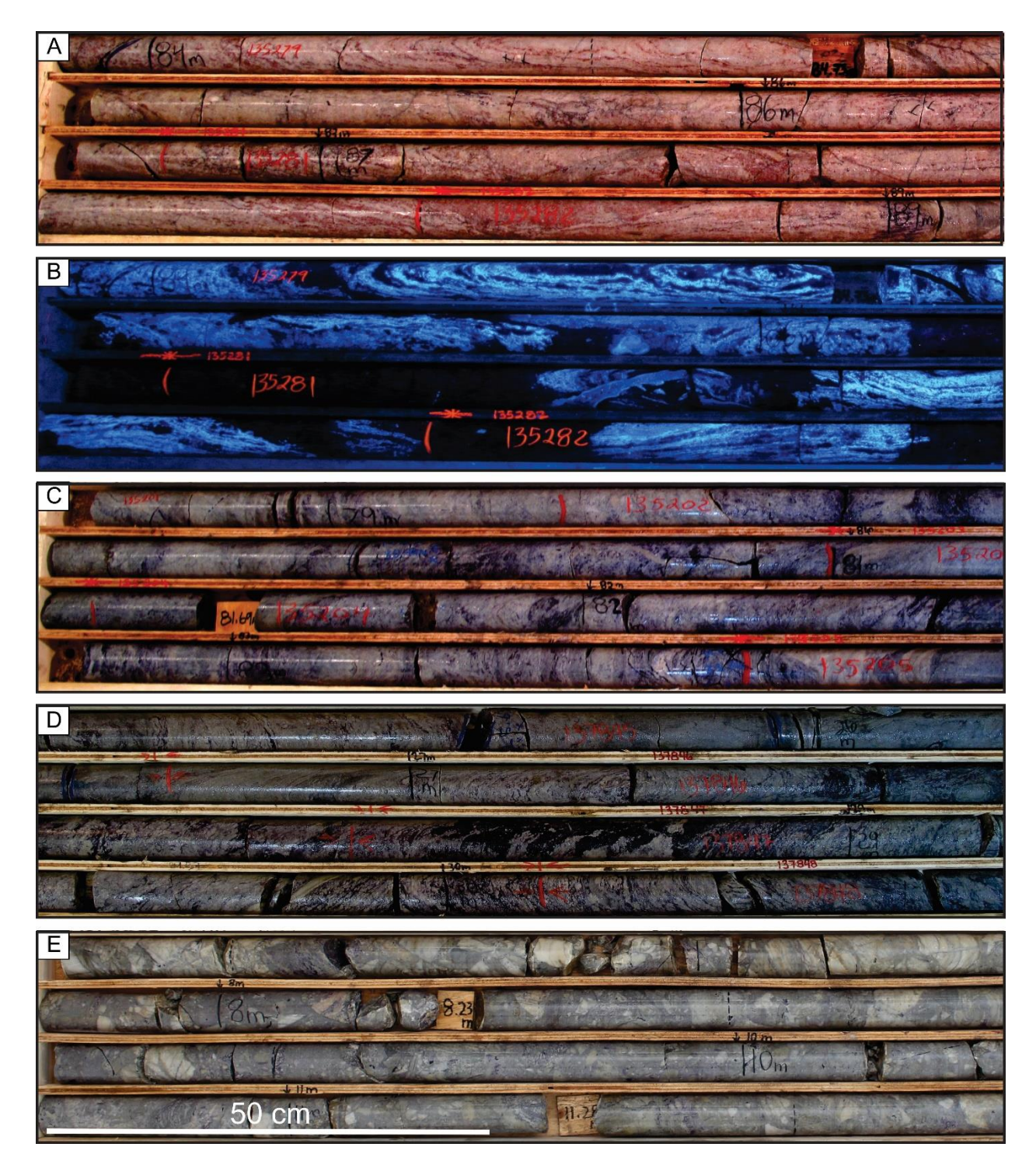


Fig. 3: Representative photographs of the various lithologies of the Ashram deposit. All drill core is 4.76 cm in diameter. A) BD zone dolomite carbonatite with pink REE-fluorocarbonate mineralization. B) The same intersection as in A) but photographed under UV light. The bright blue material is apatite. C) Weakly deformed B zone dolomite carbonatite with purple fluorite. Note the yellow tint from monazite mineralization. D) Strongly deformed A zone ferroan dolomite carbonatite with purple fluorite veinlets and patches. E) Matrix-supported polymictic breccia with fluorite ± REE-fluorocarbonates in the matrix.

Fig. 4: A three-dimensional deposit-scale distribution of selected compositional parameters relative to the breccia unit. A) Drillholes colour coded by  $P_2O_5$  (wt. %) content. All breccia intervals are overlain in black, and there is a strong alignment of intervals at the left side of the figure. Note that breccia is most commonly intersected at or near the contact with P-rich rocks. B) Drillholes colour-coded by TREE (wt %) content. The aligned intersections were modeled as a plane, overlain in black. The planar section of the breccia underlies high TREE values. C) Drillholes colour coded by MHREE/TREE ratios. The planar section of the breccia underlies the zone of MHREE-enrichment, which is highlighted by the black dashed circle. Comparison of B) and C) reveals that the apparent peripheral MHREE-enrichment in C) is unmineralized (B) and is the signature of silicate minerals in the wall-rock. All sections were prepared using Leapfrog Geo software from Seequent.

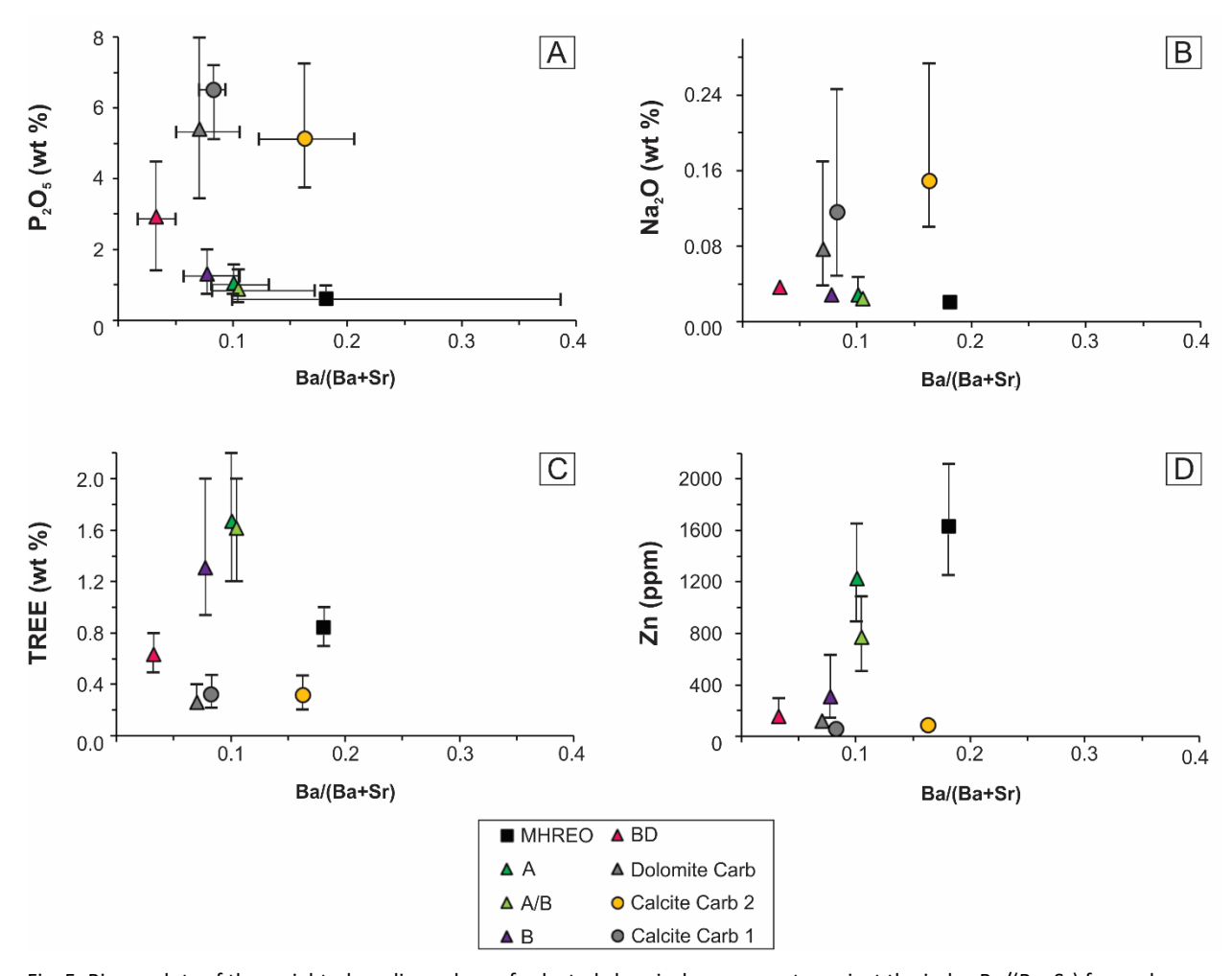


Fig. 5: Binary plots of the weighted median values of selected chemical components against the index Ba/(Ba+Sr) for each lithology of the Eldor carbonatite complex, with  $1^{st}$  and  $3^{rd}$  quartile bars shown. Median values were calculated from the results of analyses of thousands of 1 to 2 m drill core samples of variable homogeniety for each lithology. In some cases for components on the y-axis, the quartile bars are smaller than the symbol size and are therefore not shown. For simplicity, quartile bars for the x-axis are plotted on the first diagram only.

Fig. 6: Representative images of brittle carbonate textures. Points and text in yellow correspond to analyses of carbonate compositions given in Table 3. A) CL-image of coarse-grained BD zone dolomite luminescing bright red, mantled by ferroan dolomite (dark, no CL response). B) BSE image of brecciated BD zone dolomite crystals with two generations of more Fe-rich dolomite between them. C) BSE image of Rim dolomite carbonatite showing early, brecciated dolomite crystals mantled by a more Fe-rich (brighter) dolomite, and finally a limpid dolomite generation associated with apatite and pyrochlore. D) BSE image of brecciated siderite crystals of the MHREO zone carbonatite, mantled by magnesian siderite. Vugs are infilled with quartz and dolomite showing complex internal textures. White grains are monazite-(Nd) clearly associated with siderite and magnesian siderite. E) BSE image of complex siderite compositional variations and late quartz and dolomite in the MHREO zone. F) Transmitted light photomicrograph of coarse-grained siderite crystals in a matrix of finer-grained dolomite, quartz, and magnetite. Brown discolouration of dolomite is associated with monazite-(Nd) mineralization.

Fig. 7: Representative images of carbonate textures from the B and A zone carbonatites. A) Transmitted light photomicrograph of mosaic-textured medium-grained dolomite. Sample taken from the B zone. B) Transmitted light photomicrograph of deformed (sheared) dolomite carbonatite. Two distinct directions of deformation (traced in red dashed lines) are displayed in this sample taken from the A zone. C) Transmitted light photomicrograph of fine-scale textural variations. Mosaic-textured carbonates (center) are juxtaposed by a narrow band of sheared carbonate with pyrite, fluorite, and monazite (right, outlined in red dashed lines), and are crosscut by a ptygmatic vein of phlogopite, fluorite, and monazite (left). The sample was taken from the A zone. D) BSE image of three generations of A zone dolomite with interstitial siderite. E) BSE image of three generations of B zone dolomite. Monazite-(Ce) (bright white) is associated with later (light grey) dolomite. F) BSE image of a vug in dolomite carbonatite. Early vug dolomite prisms project into the cavity which was later infilled with ferroan dolomite. The sample was taken from the A zone.

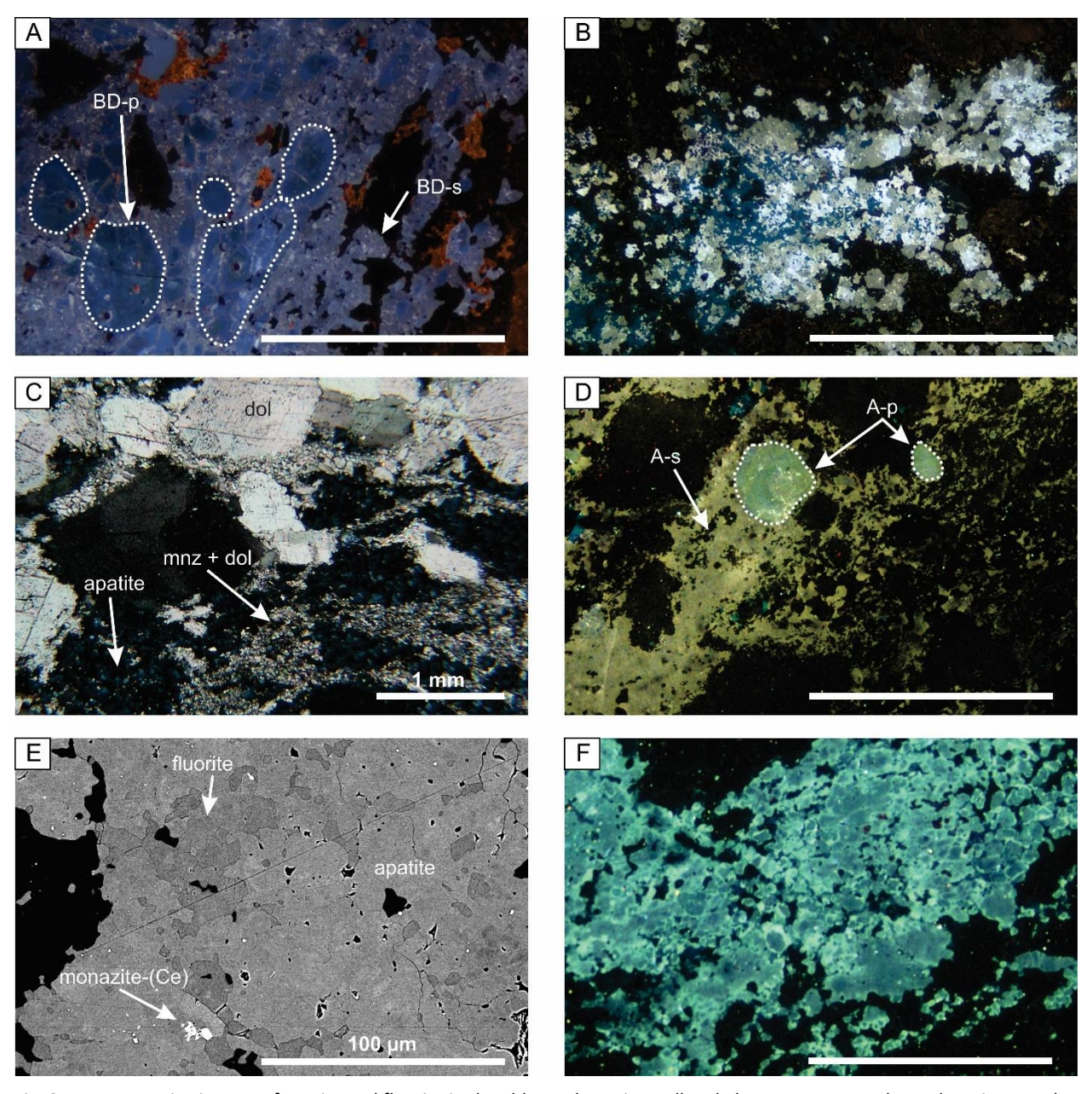


Fig. 8: Representative images of apatite and fluorite in the Eldor carbonatites. All scale bars are 1 mm, unless otherwise noted. A) A CL image of two types of apatite in the BD zone. Primary apatite (dashed white outline) is coarse-grained, ovoid and violet-luminescent. Secondary apatite is fine-grained, sucrosic and pale pink to violet luminescent. Note that the same primary apatite is ubiquitous in the Rim zone and only rarely has secondary overgrowths. B) A CL image of apatite from the B zone. White to pale violet luminescent B type apatite is intimately intergrown with fine-grained, royal blue-luminescent fluorite. C) A cross-polarized transmitted light photomicrograph of coarse-grained dolomite crystals in a matrix of fine-grained, sucrosic, recrystallized apatite with bands of fine-grained, intergrown monazite-(Ce) and dolomite. The sample was taken from the B zone. D) A CL image of two types of apatite in the A zone. Primary apatite (dashed white outline) is coarse-grained, ovoid and has a pale greenish-blue luminescence. Secondary apatite is fine-grained, sucrosic and pale yellow luminescent. E) A BSE image of apatite with very fine-grained monazite-(Ce) inclusions (white) and patchy intergrown fluorite. The sample was taken from the B zone. F) A CL image of darker, blue-green-luminescent fluorite mantled by a later, bright green-luminescent generation. The sample was taken from the A zone.

11

12

1

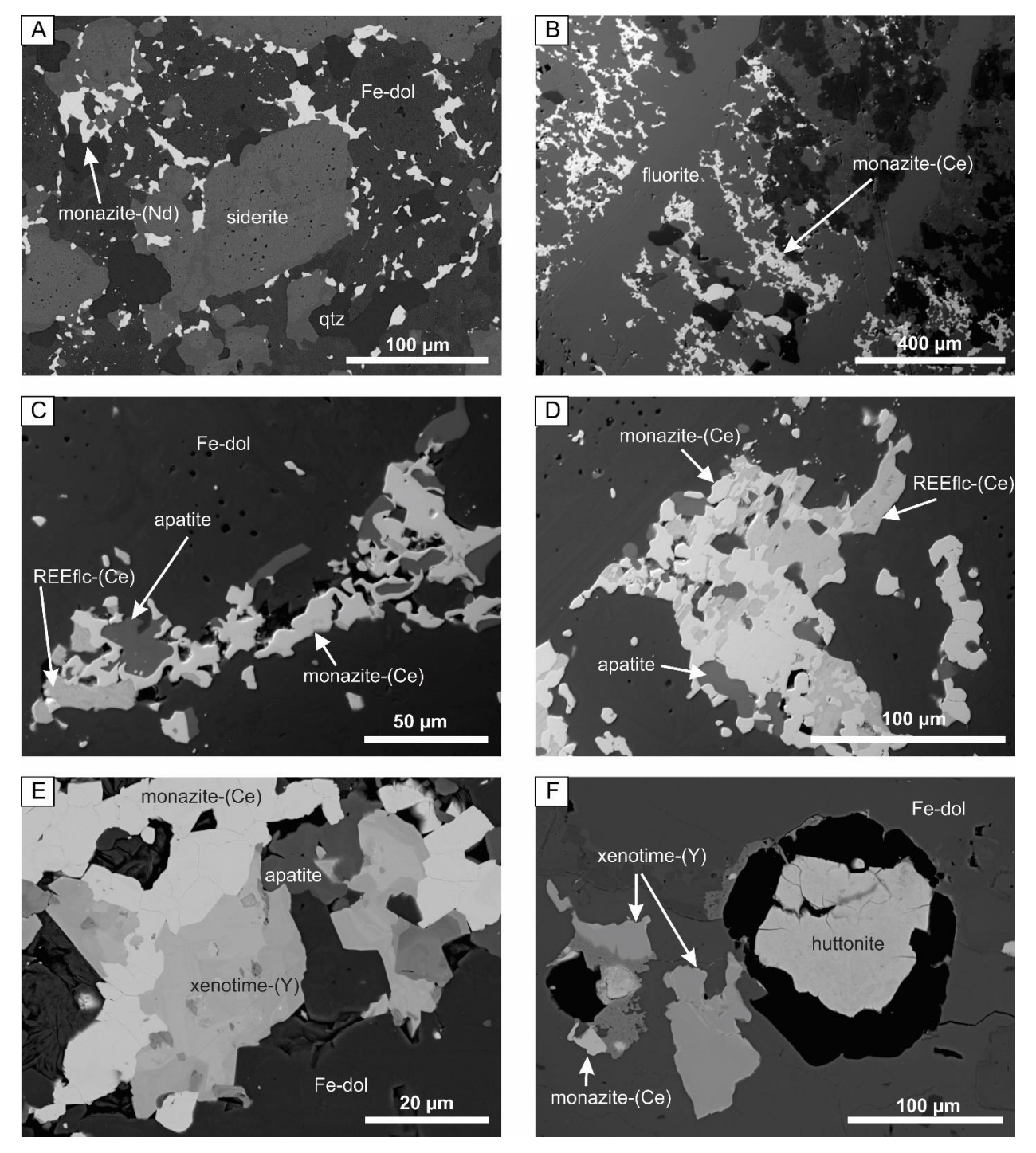


Fig. 9: Back-scattered electron images of REE minerals, their textures and paragenetic relationships. A) Monazite-(Nd) of the MHREO zone at the margins of siderite crystals. B) Veins of fluorite and monazite-(Ce) crosscut by a later generation of fluorite veins. The sample was taken from the B zone. C and D) Rare samples showing the relationships between apatite, monazite-(Ce) and the REE-fluorocarbonate minerals (REEflc-(Ce)). Apatite is mantled by monazite-(Ce) which, in turn, is mantled by REE-fluorocarbonates. The samples were taken from the BD zone. E) A rare sample showing the relationship between the different phosphates. Apatite was earliest, followed by monazite-(Ce), which is mantled by xenotime-(Y). The sample was taken from the A zone. F) Altered huttonite of the MHREO zone that is spatially associated with xenotime-(Y) and monazite-(Ce).

Fig. 10: Representative images of monazite mineralization and its paragenetic relationships. A) BSE image from A zone carbonatite with patches of monazite-(Ce) and fluorite cut by a folded phlogopite veinlet. B) Late barite associated with magnetite, bafertisite, and monazite-(Nd) in the MHREO zone. C) A BSE image showing a rare occurrence of zoned monazite crystals. The sample was taken from the A zone. The area outlined in red represents the area shown in Figs D-F. D) A BSE image of the area of interest at higher magnification. E) An EDS La distribution map of the area of interest. F) An EDS Th distribution map of the area of interest.

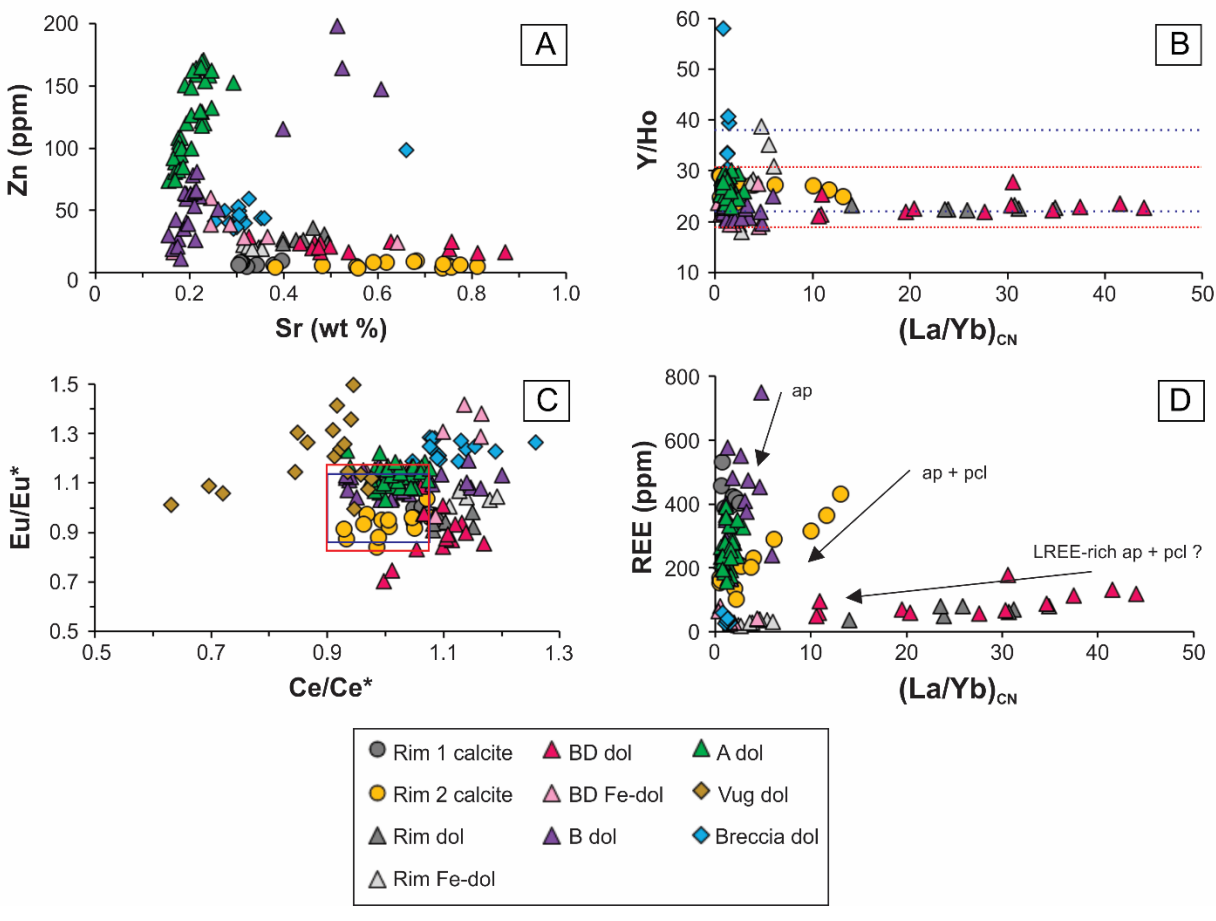


Fig. 11: Trace element compositions of calcite and dolomite across the Eldor carbonatite complex. The REE data were normalized to CI chondrite (McDonough and Sun, 1995). The fields outlined in blue and red in Figs B) and C) are the typical ranges in REE composition of primary calcite and dolomite, respectively, defined by Chakhmouradian et al. (2016b). Trends in D) are inferred evolutionary trends (see text for further detail).

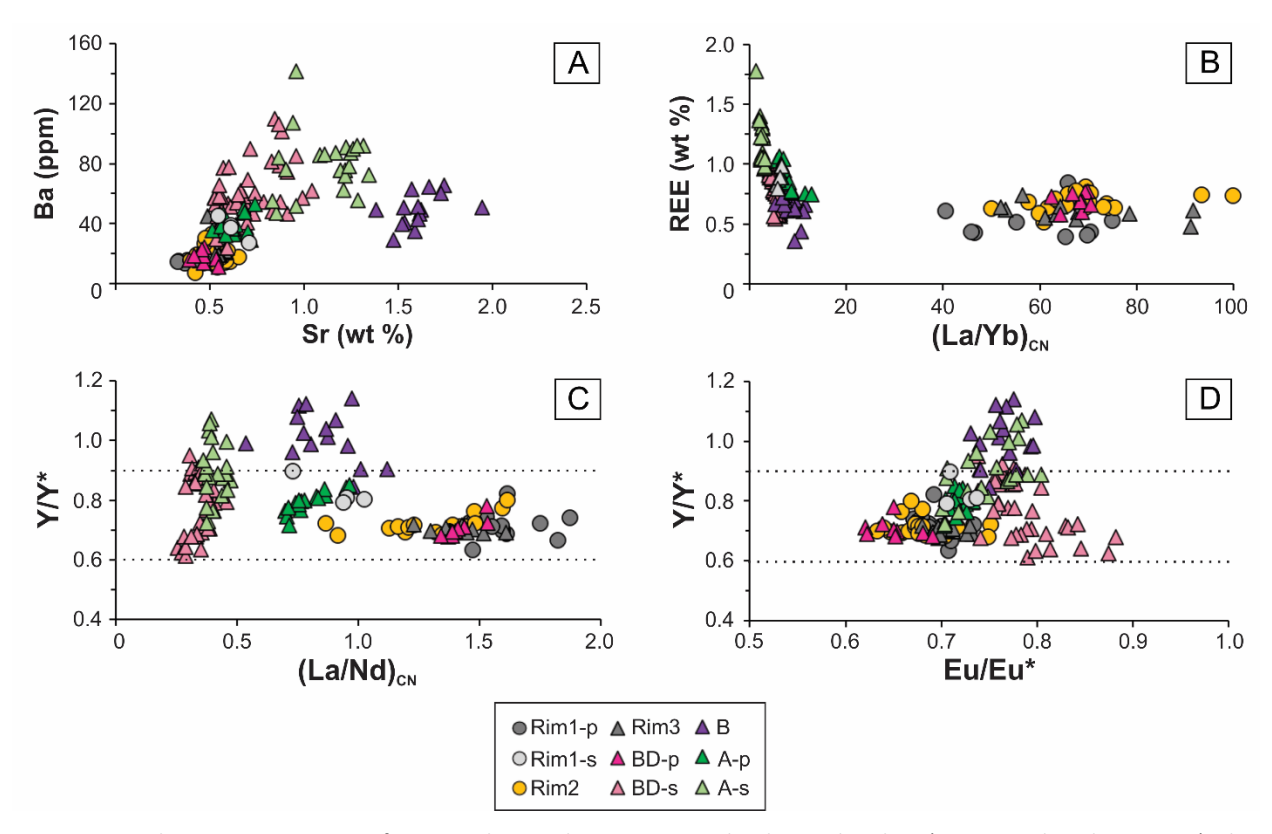


Fig. 12: Trace element compositions of apatite. The REE data were normalized to CI chondrite (McDonough and Sun, 1995). The dashed lines in C) and D) define the typical ranges in Y/Y\* of igneous apatite defined by Chakhmouradian et al. (2017).

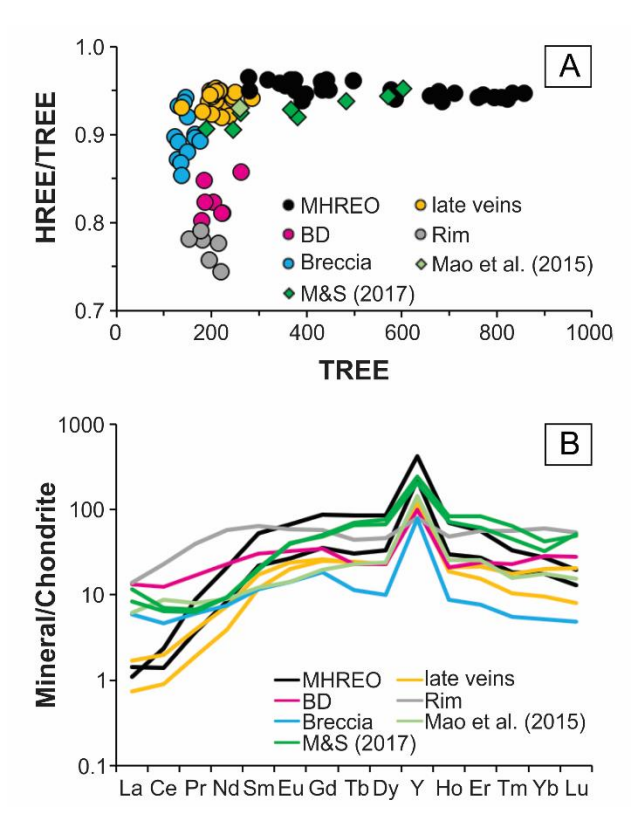


Fig. 13: Fluorite REE compositions from the current study. Included for comparison are analyses of A zone fluorite from Mao et al. (2015) and Mitchell and Smith (2017). A) HREE-enrichment (HREE/TREE) as a function of TREE content (ppm). B) A chondrite-normalized REE diagram for the average composition of each fluorite sample. The data were normalized to CI chondrite (McDonough and Sun, 1995).

2 3 4

5

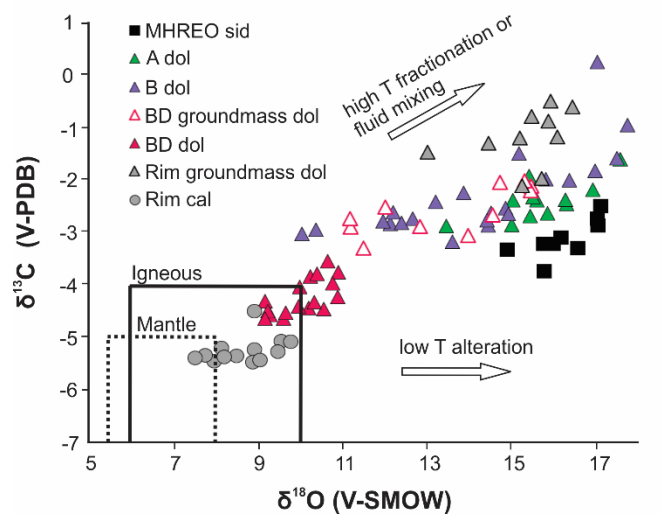
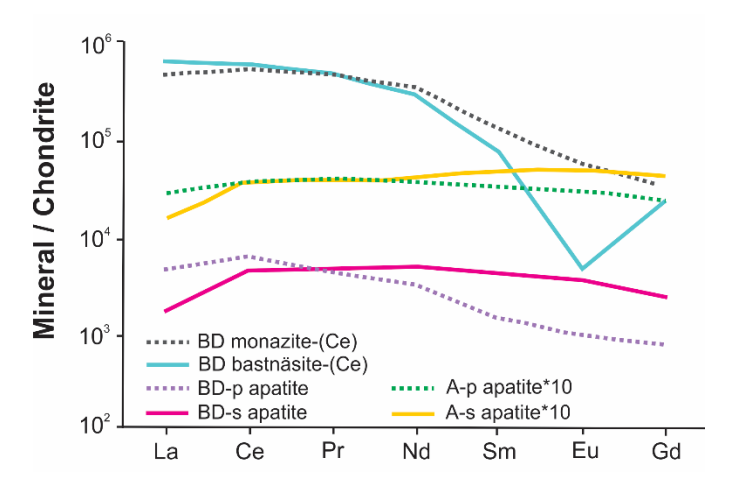


Fig. 15: A plot of  $\delta^{13}$ C V-PDB versus  $\delta^{18}$ O V-SMOW showing the distribution of carbon and oxygen isotope ratios for each lithofacies of the Eldor carbonatite complex. Also shown are the fields of mantle and primary magmatic carbonatite, after Deines (1989) and Taylor et al., (1967), respectively, and trends of low temperature alteration and high temperature fractionation/fluid mixing from Deines (1989).



2 3 4

5

Fig. 16: Chondrite-normalized REE profiles of BD zone reactants and products, and the two generations of A zone apatite. The reactant phases are shown in dashed lines, and the product phases in solid lines. The values for A zone apatite have been multipled by 10 to prevent crowding on the plot. The data are normalized to CI chondrite (McDonough and Sun, 1995).

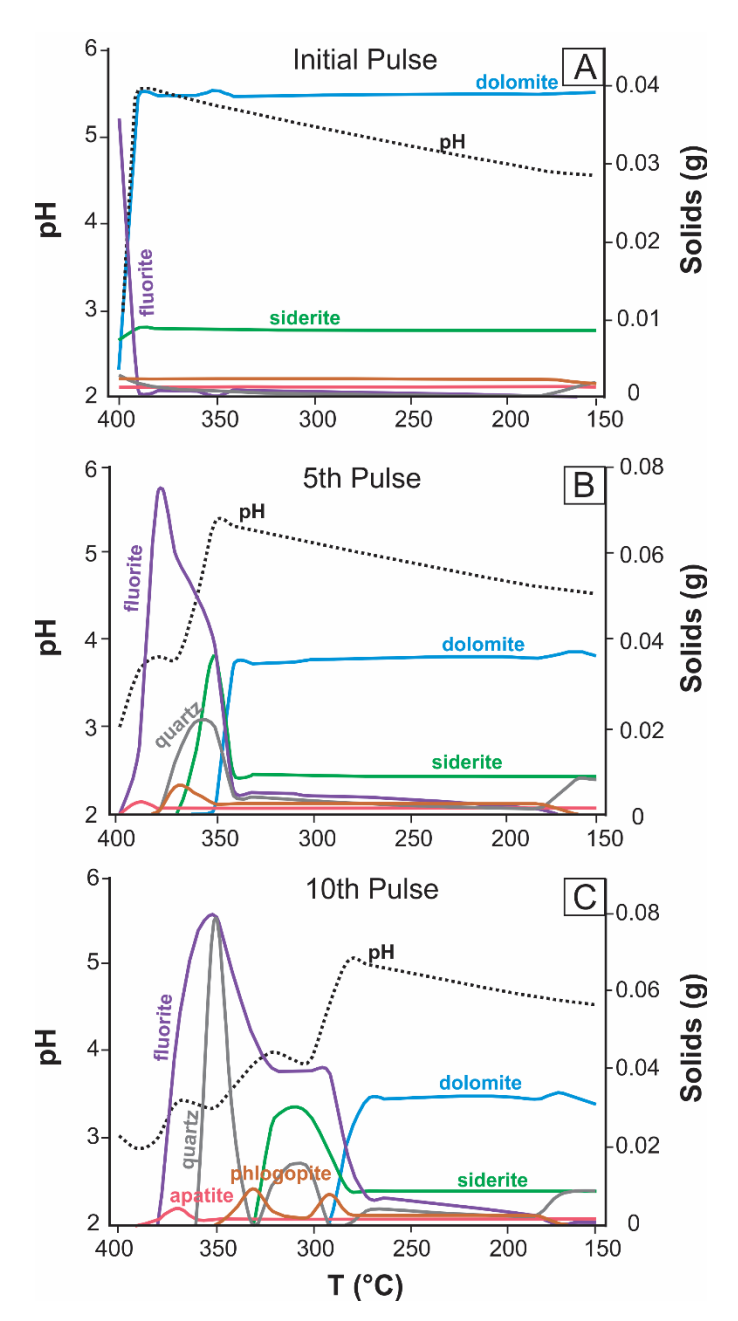


Fig. 17: The pH of fluid and mass of solids precipitated (g) as a function of temperature (°C) after interaction of a H2O-CO2 fluid with its carbonatite host rock, following A) the initial pulse of fluid, B) the 5th fluid pulse and C) the 10th pulse of fluid. The fluid contains 10 wt % NaCl, 5 wt % KCl and is undersaturated in F and SiO2. The initial pH of the fluid is 3, and interaction occurs under a constant pressure of 500 bars. See text for further detail.

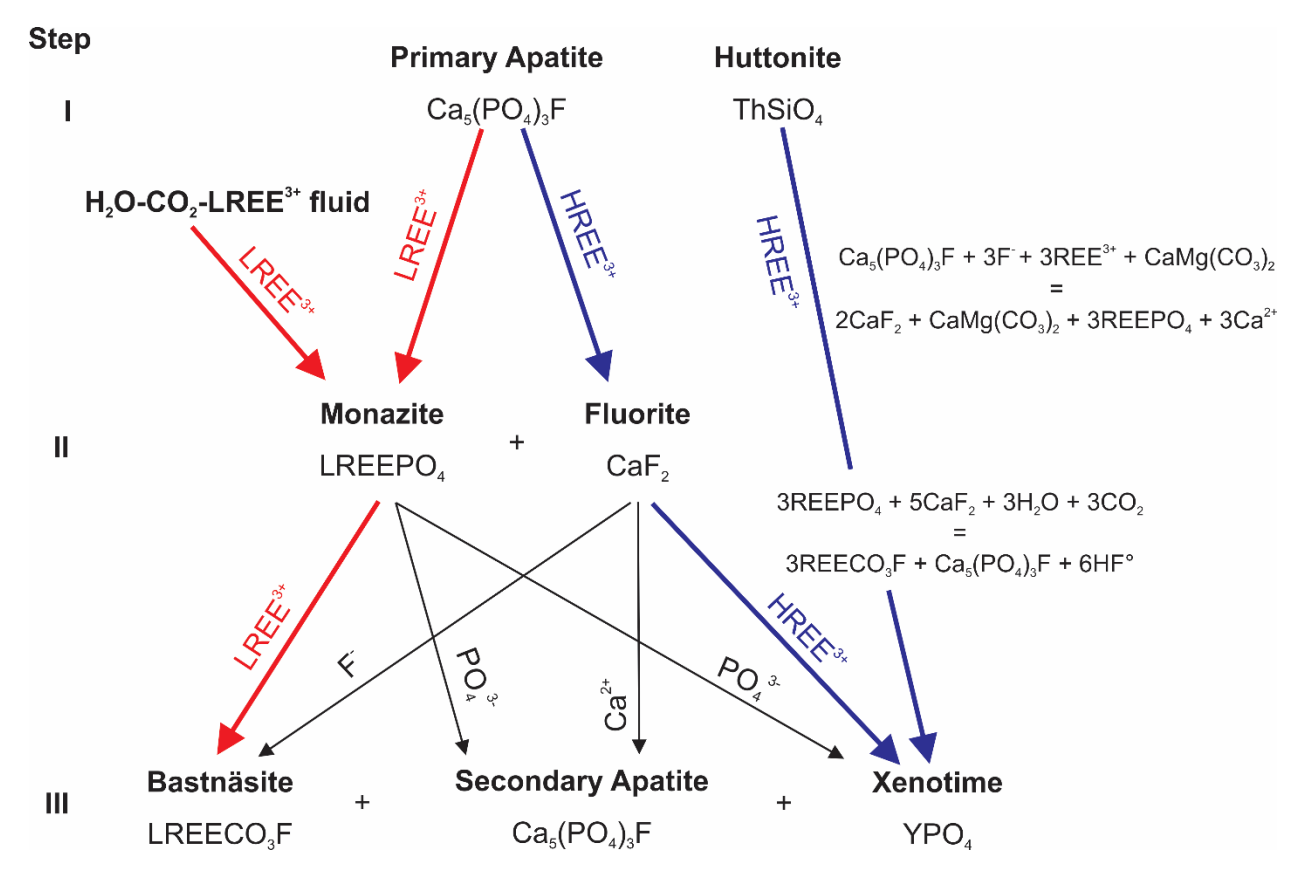


Fig. 18: A schematic diagram tracing the sources of components for the various REE-minerals and the corresponding reactions. See text for further detail.

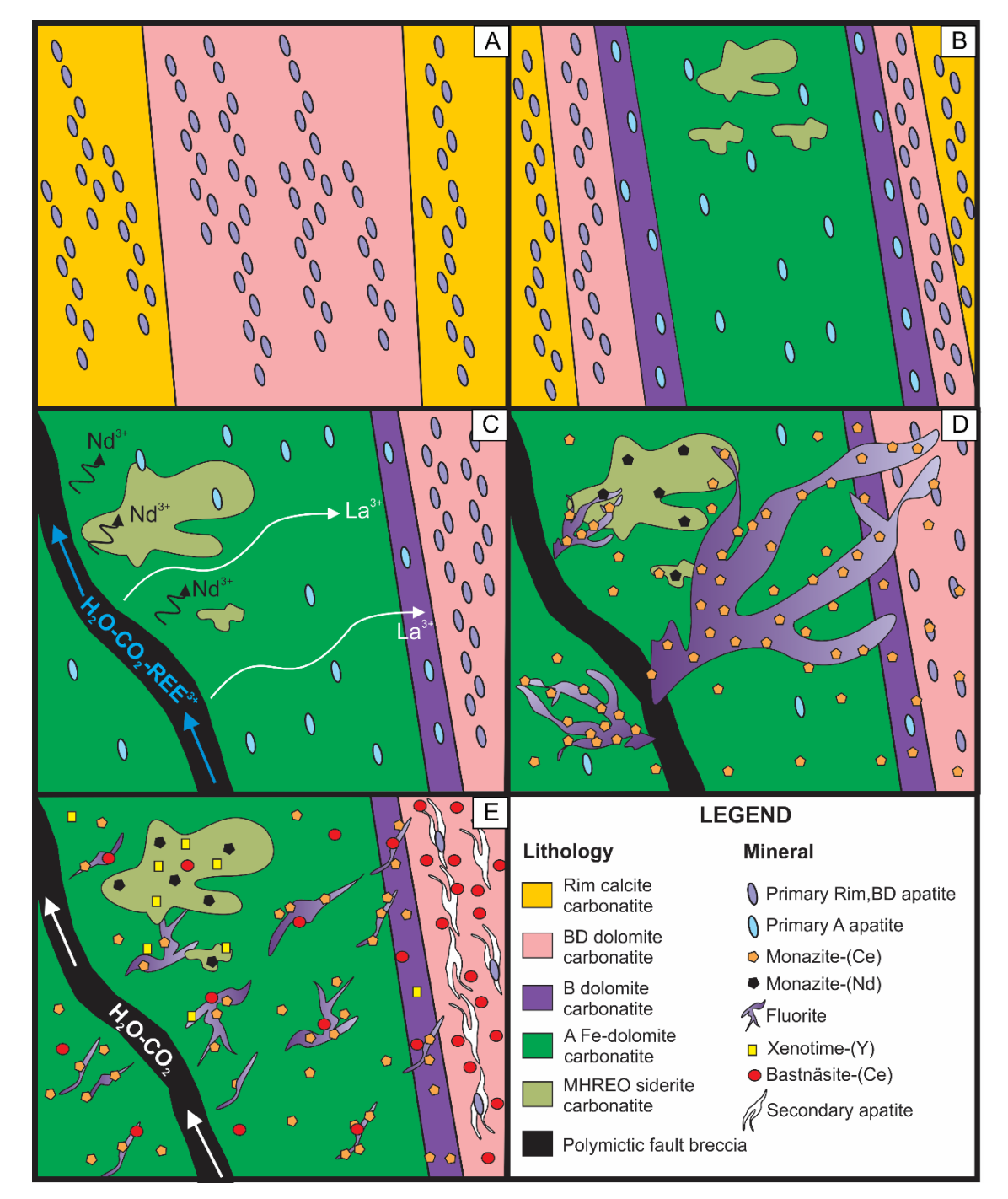


Fig. 19: A schematic diagram summarizing the proposed genetic model for the Ashram deposit. A) Stage 1: Emplacement of the primary apatite-rich Rim calcite carbonatite and BD zone dolomite carbonatite. B) Stage 2: Emplacement of the phosphate-poor Ashram carbonatite magma that differentiated magmatically to form the B, A and MHREO zone carbonatites. Note the difference in the apatite abundance of the Stage 1 and Stage 2 carbonatites. C) Faulting and brecciation accompanied by exsolution of a H<sub>2</sub>O-CO<sub>2</sub>-REE<sup>3+</sup> fluid from the Stage 2 carbonatite, and its transport up the breccia plane and into the surrounding carbonatite. Fractionation of the REE leading to the more distal mobilization of La<sup>3+</sup> relative to Nd<sup>3+</sup>. D) Deposition of fluorite and monazite at the expense of primary apatite (Reaction 1). Monazite-(Nd) is only deposited in MHREO siderite, proximal to the breccia. Replacement of apatite by monazite is nearly complete in the B, A and MHREO zones, and partial in the BD zone. E) Later, REE-barren H<sub>2</sub>O-CO<sub>2</sub> fluid partially replaces monazite-(Ce) and fluorite in the B and A zones, depositing bastnäsite-(Ce) and lesser xenotime-(Y) (Reaction 4). In the BD zone, monazite-(Ce) is completely replaced by bastnäsite-(Ce) and Rim-type apatite is replaced by secondary BD-type apatite.

	MUDEO		-	55	Calcite	Calcite
Unit	MHREO	Α	В	BD	Carbonatite 2	Carbonatite 1
TREO (wt %)	1.6	1 – 3+	1 – 2	0.6 - 1.0	-	-
MHREE/TREE (%)	≤ 20	~ 6	~ 4	~ 7	-	-
Principal REE Minerals	monazite-(Nd), monazite-(Ce), xenotime-(Y)	monazite-(Ce)	monazite-(Ce)	REE- fluorocarbonates	-	-
Fe <sub>2</sub> O <sub>3</sub> (wt %)	29.33	14.36	6.47	4.42	5.45	6.60
Principal Carbonate	siderite	Fe-dolomite	dolomite	dolomite	calcite	calcite
P <sub>2</sub> O <sub>5</sub> (wt %)	0.62	1.04	1.31	2.92	5.14	6.51
Phosphate Phase	monazite-(Nd), monazite-(Ce), xenotime-(Y)	monazite-(Ce)	monazite-(Ce)	apatite	apatite	apatite
F (wt %)	0.58	4.25	1.16	0.61	-	-
Fluorine Phase	fluorite	fluorite	fluorite	REEflc	phlogopite, apatite	phlogopite, apatite

Unit	В	Α		MHREO	
Sample	CV15018	CV16007	CV15013	CV15014	CV15301
Analysis #	366	6-1	2-7	1-2	1-1
$Nd_2O_3$	-	-	0.29	0.31	0.40
$Sm_2O_3$	0.42	0.79	1.64	1.34	0.76
$Eu_2O_3$	-	0.57	1.03	0.95	0.69
$Gd_2O_3$	3.58	4.63	5.98	6.21	5.47
$Tb_2O_3$	1.13	1.13	1.49	1.18	1.44
$Dy_2O_3$	9.10	9.28	9.17	7.62	10.57
$Y_2O_3$	40.73	37.57	35.95	39.10	34.90
$Ho_2O_3$	1.58	1.55	1.45	1.17	1.95
Er <sub>2</sub> O <sub>3</sub>	3.55	3.99	3.21	2.11	4.19
$Tm_2O_3$	0.44	0.54	0.41	0.22	0.48
$Yb_2O_3$	2.42	3.05	2.15	1.00	2.42
Lu <sub>2</sub> O <sub>3</sub>	0.22	0.41	0.28	0.11	0.23
$ThO_2$	-	0.61	1.28	0.26	0.36
CaO	0.41	0.14	0.20	0.41	0.28
$P_2O_5$	35.65	35.25	34.96	37.98	34.86
F	0.67	0.40	0.35	0.36	0.36
SiO <sub>2</sub>	-	-	0.24	0.28	0.16
FeO	0.39	0.31	0.36	0.45	0.07
Total	100.89	100.23	100.39	100.91	99.43
-O=F	-0.28	-0.17	-0.15	-0.15	-0.15
Total	100.61	100.06	100.24	100.76	99.27
Nd	0.002	<b>O=</b> 0.001	• <b>4</b> 0.004	0.004	0.005
Sm	0.002	0.001	0.004	0.004	0.005
Eu	0.000	0.003	0.013	0.013	0.008
Gd	0.039	0.052	0.068	0.066	0.062
Tb	0.012	0.013	0.017	0.013	0.016
Dy	0.097	0.101	0.101	0.079	0.117
Υ	0.719	0.678	0.652	0.672	0.639
Но	0.017	0.017	0.016	0.012	0.021
Er -	0.037	0.042	0.034	0.021	0.045
Tm	0.005	0.006	0.004	0.002	0.005
Yb Lu	0.025 0.002	0.032 0.004	0.022 0.003	0.010 0.001	0.025 0.002
Th	0.002	0.004	0.003	0.001	0.002
Ca	0.015	0.005	0.017	0.002	0.000
P	1.001	1.012	1.008	1.038	1.015
F	0.069	0.043	0.038	0.036	0.039
Si		0.003	0.008	0.009	0.005
Pb			0.001		
Fe	0.011	0.009	0.010	0.012	0.002
total	2.055	2.037	2.033	2.016	2.030

Sample	15001- 104	15014- 140	15014- 125	15014- 107	15014- 114	15014- 132	15014- 146
La <sub>2</sub> O <sub>3</sub>	-	-	0.25	0.24	-	-	0.23
Ce <sub>2</sub> O <sub>3</sub>	0.47	0.53	0.70	0.54	0.50	0.64	1.09
Pr <sub>2</sub> O <sub>3</sub>	-	0.20	-	0.20	-	-	0.29
Nd <sub>2</sub> O <sub>3</sub>	1.20	1.60	1.42	1.22	0.81	1.14	1.84
Sm <sub>2</sub> O <sub>3</sub>	0.85	1.08	0.80	0.75	0.52	0.81	0.61
$Eu_2O_3$	-	-	-	-	-	-	-
$Gd_2O_3$	1.55	1.71	0.99	0.93	0.78	1.17	0.93
$Tb_2O_3$	0.46	0.24	-	-	-	-	0.16
$Dy_2O_3$	3.48	1.50	0.89	0.96	0.54	1.24	0.60
$Y_2O_3$	12.32	7.08	3.85	3.85	2.40	5.45	2.41
Ho <sub>2</sub> O <sub>3</sub>	0.60	0.26	-	-	-	-	-
			0.29	0.27	_		0.28
Er <sub>2</sub> O <sub>3</sub>	1.55	0.56				0.55	
Tm <sub>2</sub> O <sub>3</sub>	-	-	-	-	-	-	-
$Yb_2O_3$	1.10	0.36	0.21	0.16	0.12	0.36	0.08
Lu <sub>2</sub> O <sub>3</sub>	-	-	-	0.11	-	-	-
ThO <sub>2</sub>	38.58	43.96	45.13	45.59	47.82	49.99	58.49
$UO_2$	-	-	-	-	-	-	-
CaO	1.38	1.15	2.59	2.61	2.59	2.58	5.23
$P_2O_5$	5.45	3.37	2.36	2.14	1.26	2.58	2.05
F	0.74	0.76	0.55	-	-	-	-
SiO <sub>2</sub>	12.54	12.92	9.25	8.14	9.30	8.22	8.09
PbO	_	-	-	-	-	-	_
FeO	3.53	8.66	8.11	13.17	12.42	5.35	12.78
Na₂O	_	-	_	_	_	_	_
TiO <sub>2</sub>	-	0.25	0.35	0.75	_	0.24	0.13
<del>-</del>	0.43	0.74	0.63	1.03	0.52	0.85	0.75
Ta <sub>2</sub> O <sub>5</sub>	-	- 07.01	- 70.64	- 02.24	-	-	-
Total	86.43 23.57	87.21 15.12	78.64 9.40	83.24 9.22	80.30 5.66	82.05 11.36	96.25 8.53
TREO	23.31	13.12			3.00	11.30	0.55
_			0 =	-			
La			0.004				0.003
Ce	0.006	0.007	0.011	0.008	0.008	0.010	0.015
Pr	0.045	0.003	0.000	0.003	0.040	0.040	0.004
Nd Con	0.015	0.021	0.022		0.013	0.018	0.025
Sm	0.010	0.014	0.012	0.011	0.008	0.012	0.008
Eu	0.018	0.021	0.014	0.013	0.011	0.017	0.010
Gd Tb	0.018	0.021	0.014	0.013	0.011	0.017	0.012 0.002
Dy	0.003	0.003	0.013	0.013	0.008	0.017	0.002
Y	0.234	0.010	0.013	0.013	0.056	0.017	0.007
Ho	0.007	0.003	0.000	0.000	0.000	0.127	0.040
Er	0.017	0.007	0.004	0.004		0.008	0.003
Tm	0.0	0.00.	0.00	0.00		0.000	0.000
Yb	0.012	0.004	0.003	0.002	0.002	0.005	0.001
Lu				0.001			
Th	0.313	0.367	0.449	0.434	0.477	0.498	0.509
U							
Ca	0.053	0.045	0.121	0.117	0.122	0.121	0.215
P	0.165	0.105	0.087	0.076	0.047	0.096	0.067
F	0.081	0.085	0.074				
Si	0.448	0.474	0.404	0.341	0.408	0.360	0.310
Pb							
Fe	0.105	0.266	0.296	0.461	0.456	0.196	0.409
Na							
Ti		0.007	0.012	0.023		0.008	0.004
Nb	0.007	0.012	0.012	0.019	0.010	0.017	0.013
Ta	:					4	
Total	1.544	1.606	1.637	1.677	1.673	1.567	1.667

			Stage 2				Sta	ge 1	
			Ashra	m				Rim	
	MHREO	A	A/B	В	Breccia	BD	Dol Carb	Calcite Carb 2	Calcite Carb 1
Length (m)	97.36	4187.61	5084.45	669.29	193.03	1783.19	1777.02	224.75	25.90
SiO <sub>2</sub>	1.64	1.96	1.57	1.99	2.74	0.88	1.88	1.95	3.62
$Al_2O_3$	0.06	0.10	0.07	0.05	0.43	0.06	0.42	0.23	0.20
Fe <sub>2</sub> O <sub>3</sub> (total)	29.33	14.36	9.53	6.47	10.85	4.42	7.43	5.45	6.60
MnO	2.58	1.89	1.42	1.28	0.93	0.78	0.53	0.39	0.66
MgO	7.78	12.99	13.34	16.27	14.07	16.57	16.02	4.57	8.72
CaO	12.60	29.25	27.35	30.11	28.23	31.20	37.80	58.62	76.34
Na <sub>2</sub> O	0.02	0.03	0.02	0.03	0.06	0.04	0.08	0.15	0.12
K <sub>2</sub> O	0.03	0.06	0.05	0.04	0.29	0.04	0.26	0.18	0.19
TiO <sub>2</sub>	0.27	0.19	0.10	0.05	0.56	0.03	0.16	0.11	0.16
P <sub>2</sub> O <sub>5</sub>	0.62	1.04	0.88	1.31	2.88	2.92	5.41	5.14	6.51
F	0.58	4.25	1.98	1.16	0.46	0.61	-	-	-
Sc	30	59	40	49	34	22	13	11	10
V	107	78	69	60	113	37	163	79	10
Со	14	7	6	5	16	2	13	6	10
Zn	1633	1228	768	310	531	158	117	89	57
Sr	960	2394	2384	2681	2995	3561	1981	4693	5484
Υ	235	441	241	166	238	166	126	120	156
Zr	5	35	18	65	64	40	198	101	156
Nb	302	516	349	268	794	214	1796	210	3216
Мо	0	6	5	9	3	5	5	10	12
Sn	24	22	10	5	11	2	4	2	4
Ва	212	268	279	226	189	121	150	913	493
La	1066	3944	4113	3086	1688	1150	495	604	600
Ce	3392	7581	7600	6099	3329	2750	1129	1392	1481
Pr	536	816	789	683	400	348	140	166	163
Nd	2412	2940	2710	2452	1502	1426	533	658	621
Sm	389	428	333	298	219	212	73	100	87
Eu	90	106	76	64	52	51	20	26	24
Gd	197	244	182	144	125	117	55	63	60
Tb	19	28	17	12	14	12	6	7	8
Dy	70	114	66	45	63	49	30	32	36
Но	9	16	9	6	9	7	5	5	6
Er _	19	34	19	13	22	14	11	12	14
Tm	2	4	2	2	3	2	1	1	2
Yb	12	20	12	10	14	9	8	8	10
Lu	1	3	2	1	2	1	1	1	1
Hf To	1	1	1	1	1	1	2	1	2
Ta w	0	0	0 2	0	1	0	42 3	12	54
W	1	4		1	4	0		0	1
Pb	747	226	110	25	159	29	19	38	15

## © 2021. This manuscript version is made available under the CC-BY-NC-ND 4.0 license http://creativecommons.org/licenses/by-nc-nd/4.0/

		ı	Rim													Ashram										
Unit	Cal Carb 1	Cal Carb 2	ı	Dol Carb	,		BD			В						A							MHREO			
Sample	CV15029	CV15050		CV15109	)		CV15115	;		CV15141				CV15005	;			CV16007			CV1	5339			CV15337	•
Mineral	cc	cc	dol1	dol2	dol3	dol1	dol2	dol3	dol1	dol2	dol3	dol1	dol2	dol3	sid1	sid2	dol1	dol2	dol3	sid1	sid2	sid3	sid4	dol1	dol2	ank
	gm	gm	gm	gm	gm	gm	gm	gm	gm	gm	gm	gm	gm	gm	gm	gm	vug	vug	vug	gm	gm	gm	gm	vug	vug	vug
CaO	54.50	52.44	29.66	28.34	29.36	28.78	28.78	28.78	28.59	28.65	28.60	27.13	28.33	27.92	0.74	0.26	28.96	28.17	28.57	0.43	0.49	0.06	0.07	29.21	27.43	27.04
MgO	0.10	1.03	20.22	16.95	16.64	20.77	14.53	17.20	20.22	18.84	17.01	14.65	19.01	13.63	18.03	13.54	18.71	12.34	15.62	2.75	4.70	7.84	11.79	17.18	11.01	8.15
FeO	0.56	0.51	1.15	3.98	6.62	1.03	9.65	5.99	2.02	3.49	5.21	7.56	3.47	11.20	35.07	39.14	4.24	12.83	8.27	53.61	50.01	48.24	42.92	6.37	15.12	19.01
MnO	0.64	0.20	0.76	2.97	0.49	0.48	1.35	0.73	0.47	0.61	1.67	1.35	0.33	1.76	4.02	4.21	0.49	1.87	1.21	4.17	4.59	4.19	4.42	0.80	1.50	2.02
SrO	0.29	0.76	0.48	0.30	0.09	1.25	0.08	0.50	0.64	0.75	0.20	0.14	0.68	0.22	-	-	0.06	0.31	0.44	-	-	-	-	-	0.53	0.32
$Al_2O_3$	-	0.04	-	-	-	-	-	0.02	0.02	-	-	-	0.03	-	-	-	0.03	-	0.02	0.02	-	-	-	0.03	-	-
BaO	-	0.03	0.05	0.14	-	0.05	0.03	0.14	0.08	-	-	-	0.09	-	0.06	0.09	-	-	-	0.07	-	-	-	-	0.09	0.06
CO2	43.92	44.99	47.66	47.32	46.81	47.62	45.59	46.64	47.97	47.67	47.32	49.16	48.05	45.26	42.04	42.76	47.51	44.47	45.88	38.93	40.19	39.66	40.79	46.41	44.34	43.40
Total	100.00	100.00	100.00	100.00	100.00	100.00	100.00	100.00	100.00	100.00	100.00	100.00	100.00	100.00	100.00	100.00	100.00	100.00	100.00	100.00	100.00	100.00	100.00	100.00	100.00	100.00
	0 =	= 3						0:	=6						0:	=3		O=6			0:	=3			O = 6	
Ca	0.975	0.928	0.983	0.955	0.993	0.954	0.993	0.975	0.946	0.955	0.962	0.905	0.941	0.971	0.014	0.005	0.966	0.992	0.980	0.009	0.010	0.001	0.001	0.990	0.973	0.980
Mg	0.002	0.025	0.932	0.794	0.783	0.958	0.698	0.811	0.931	0.874	0.796	0.680	0.878	0.660	0.460	0.349	0.869	0.605	0.745	0.077	0.129	0.214	0.312	0.810	0.543	0.411
Fe	0.008	0.007	0.030	0.105	0.175	0.027	0.260	0.158	0.052	0.091	0.137	0.197	0.090	0.304	0.502	0.566	0.111	0.353	0.222	0.844	0.770	0.738	0.638	0.168	0.419	0.538
Mn	0.009	0.003	0.020	0.079	0.013	0.013	0.037	0.019	0.012	0.016	0.044	0.036	0.009	0.048	0.058	0.062	0.013	0.052	0.033	0.067	0.072	0.065	0.067	0.021	0.042	0.058
Sr	0.003	0.007	0.009	0.006	0.002	0.022	0.002	0.009	0.011	0.014	0.004	0.003	0.012	0.004			0.001	0.006	0.008						0.010	0.006
Al		0.001						0.001	0.001				0.001				0.001		0.001	0.001				0.001		
Ва		0.000	0.001	0.002		0.001	0.000	0.002	0.001				0.001		0.000	0.001				0.001					0.001	0.001
С	1.001	1.014	2.013	2.030	2.018	2.012	2.005	2.013	2.023	2.025	2.029	2.090	2.034	2.006	0.983	1.009	2.020	1.996	2.006	1.001	1.010	0.991	0.991	2.004	2.006	2.004
Total	1.999	1.985	3.987	3.970	3.983	3.988	3.995	3.987	3.977	3.975	3.972	3.910	3.966	3.994	2.017	1.991	3.980	4.004	3.994	1.999	1.990	2.009	2.009	3.995	3.995	3.996
Ba C		0.000 1.014	2.013	2.030		2.012	2.005	2.013	0.001 2.023				2.034		0.983	1.009			2.006	0.001 1.001					2.006	2.004

## © 2021. This manuscript version is made available under the CC-BY-NC-ND 4.0 license http://creativecommons.org/licenses/by-nc-nd/4.0/

Unit						ВІ				В					A				MHR		Bre					
Mineral	cal								do		gm		gm		gm		gm		gm		vug		sid		de	
Sample	1502	29	150	159	151	09	151	09	151	14	160	27	160		151	27		020	150		150		150	14	160	
n			5	,	7	,	- /		5		6		16		9		22		16		10		12		16	
<b>-</b>		1σ		1σ	07.0	1σ		1σ		1σ	0.5	1σ	00	1σ		1σ	440	1σ		1σ	00	1σ		1σ	-4	1σ
Zn	7.4	1.7	5.0	2.5	27.6	4.5	20	1.4	20	4.5 1.7	35	15	69	57	58	17	113	45	142	22	62	14	282	109	51	17
Pb	14	2.3	12	8.1	11	7.4	1.5	0.4	4.4		2.3	0.6	10	6.2	14	1.4	12	1.7	16	4.1	5.3	3.2	3.7	2.2	4.6	2.8
Sr	3366	365 93	2638	1059 97	4436	385	3372	147	7636	906	2703	686	2711	1503	2043	101	1824	147	2305	214 17	2667	712	7.2	3.8	3132	1125
Ba	981		205 22		30	4.8	24 2.8	7.5	50 22	6.1 4.9	42	8.7	56 17	14	92	29	82	32	73	2.7	62	48 0.7	12	4.5	32	10 0.6
La	23	4.7 14		8.9	12	3.7		1.0 3.2	58		2.1	1.1		13	16 60	11	11	4.1 12	8.6		1.3		0.2	0.1	1.3	
Ce	86 16	2.6	54 8	24 3.7	30 3.5	8.2 0.9	10 1.6	3.2 0.5	7.4	15 2.1	8.2 1.4	3.0 0.5	60 11	32 5.9	12	35 6.2	41 7.8	2.3	25 4.1	5.5 0.8	3.2 0.5	1.7 0.3	0.8 0.2	0.3 0.1	6.3 1.2	1.4 0.2
Pr Nd	62	2.6 10	o 34	3.7 16	3.5 10	2.8	5.4	1.6	22	7.2	6.3	2.5	56	32	54	25	7.6 39	2.3 12	20	4.0	2.4	1.2	1.5	0.1	6.0	1.2
	17	1.4	9	4.4		0.4		0.3	3.5	1.7	2.2	1.4	22	16	16	3.5	14	3.9	8.5	1.4	0.9	0.4	0.8		1.9	0.4
Sm	6.2	0.4	3	1.7	1.5 0.4	0.4	1.1 0.4	0.3	0.9	0.4	1.0	0.6	8.7	6.1	6.1	1.0	6.2	1.2	4.0	0.6	0.6	0.4	0.8	0.4 0.1	0.8	0.4
Eu	23	1.7	3 11		1.2	0.1	1.1	0.1	2.8	0.4	2.8	1.9	26	17	18	3.1	20	3.5	13	1.7	2.0	0.2	1.2	0.1	2.1	0.4
Gd Th	3.4	0.5	11	4.1 0.5	0.1	0.0	0.2	0.0	0.3	0.9	0.5	0.4	4.9	2.9	3.4	0.6	3.7	0.6	2.6	0.4	0.4	0.9	0.2		0.3	0.4
Tb	23	5.2	8	2.8	0.1	0.0	0.2	0.0	1.4	0.1	2.9	2.4	4.9 27	2.9 15	20	3.3	21	3.9	17	2.7	3.1	0.1	1.9	0.1 1.1	1.8	0.1
Dy	136	43	45	12	3.0	0.6	3.7	0.1	6.3	2.7	12	2.4 11	103	43	94	3.3 15	88	16	85	13	18	3.4	1.9	8.5	1.0	13
т Но	5.4	1.7	2	0.6	0.1	0.0	0.2	0.0	0.3	0.1	0.6	0.5	4.9	2.2	4.1	0.6	3.4	0.8	3.0	0.5	0.7	0.2	0.4	0.3	0.3	0.2
Er	15	5.9	5	1.5	0.1	0.0	0.2	0.0	0.6	0.1	1.4	1.1	10	3.8	10	1.5	7.8	1.9	7.6	1.4	2.2	0.2	1.4	0.9	0.9	0.2
Tm	2.3	1.0	1	0.2	0.3	0.0	0.4	0.0	0.0	0.0	0.2	0.2	1.2	0.3	1.2	0.2	0.9	0.2	0.9	0.2	0.3	0.7	0.2	0.9	0.5	0.0
Yb	13	6.0	1	1.5	0.1	0.0	0.1	0.0	0.5	0.0	1.2	0.2	5.7	1.1	5.7	0.2	5.3	1.3	5.5	1.1	1.8	0.1	1.4	0.1	0.1	0.7
Lu	1.8	0.9	1	0.2	0.3	0.0	0.3	0.0	0.3	0.0	0.2	0.0	0.7	0.1	0.7	0.5	0.7	0.2	0.7	0.1	0.3	0.7	0.2	0.0	0.0	0.1
Lu	1.0	0.9	'	0.2	0.1	0.0	0.1	0.0	0.1	0.0	0.2	0.1	0.7	0.1	0.7	0.1	0.7	0.2	0.7	0.1	0.5	0.1	0.2	0.1	0.1	0.1
TREE	432		207		64		28		126		43		359	1	321		272		206		37		24		35	
HREE/TREE			0.32218		0.07406		0.20561		0.07609		0.44461		0.44086		0.4329		0.48512		0.59502		0.70956		0.79083		0.44133	
Eu/Eu*	1.06413		0.9655		1.10556		1.13452		1.09986		1.09486		1.03681		1.0109		1.03295		0.99431		0.93928		0.94631		1.10677	
Ce/Ce*	0.97214		1.02563		0.94237		1.03579		0.88065		1.28072		1.1118		1.07622		1.11903		1.15266		1.22984		0.94658		1.2476	

Unit				Rim CO	2	Rim D	С		BD			В			Α			
Type	Rim1-	р	Rim1-	s	Rim2	?	Rim3	;	BD-p	)	BD-s	i	В		А-р		A-s	
Sample	15029	9	15029	9	15049	•	15109	)	15114	1	15114	Į.	1601	0	15194	1	1519	3
n	12		4		11		11		9		5		13		17		11	
		1σ		1σ		1σ		1σ		1σ		1σ		1σ		1σ		1σ
Na	945	155	1509	216	486	92	745	173	518	93	1170	87	2202	1346	1862	289	1972	483
Mn	250	55	94	27	382	392	175	24	293	158	280	450	604	247	493	450	266	67
Sr	4459	832	6163	673	4736	483	5020	584	4681	491	5859	509	16085	1306	6143	797	11232	1677
Ва	17	3	37	8	21	7	21	8	18	4	56	6	49	11	38	7	80	20
La	843	283	766	140	991	76	860	77	1000	85	349	20	556	76	678	59	375	41
Ce	2616	597	2609	329	3498	269	3016	422	3478	361	2241	79	2154	315	2227	168	2204	220
Pr	285	69	381	33	369	38	330	35	367	42	405	22	304	54	354	25	347	28
Nd	996	252	1620	131	1345	135	1167	129	1361	152	2179	238	1291	260	1629	158	1779	125
Sm	149	40	388	30	194	22	169	23	198	24	620	75	276	65	463	103	705	82
Eu	41	11	131	13	51	5	46	7	51	6	200	22	90	20	163	42	269	43
Gd	110	32	383	35	144	15	118	17	144	16	508	74	230	51	493	138	805	192
Tb	12	4	59	5	14	1	12	2	14	2	58	8	31	6	80	24	147	39
Dy	55	23	366	29	62	6	53	10	61	7	260	40	181	35	469	143	875	280
Ý	198	93	1682	140	212	15	176	33	210	18	1110	267	998	229	1809	467	3763	1096
Но	9	4	67	5	9	1	8	1	9	1	38	8	32	6	72	21	132	40
Er	19	9	167	16	20	2	17	3	20	2	82	17	80	16	141	39	255	71
Tm	2	1	18	2	2	0	2	0	2	0	8	1	9	2	13	3	23	7
Yb	9	4	85	9	10	1	9	2	10	1	42	6	45	10	59	14	104	28
Lu	1	0	9	1	1	0	1	0	1	0	5	1	5	1	6	1	12	3
TREE (ppm)	5345	ŭ	8732	•	6922	·	5984	ŭ	6927	ŭ	8106	•	6282	•	8655	•	11795	Ü

## © 2021. This manuscript version is made available under the CC-BY-NC-ND 4.0 license http://creativecommons.org/licenses/by-nc-nd/4.0/ Table 7 Fluorite Average REE

Unit			В	)		MHR	EO			Late V	eins		Bre	ccia
Sample	151	09	151	16	153	48	150	13	153	96	152	222	160	38
n	15		7		14		17		15		17		13	
'		1σ		1σ		1σ		1σ		1σ		1σ		1σ
La	3.31	0.37	3.16	0.77	0.26	0.14	0.34	0.13	0.18	0.03	0.40	0.21	1.41	0.32
Ce	13.98	3.64	7.70	1.69	1.45	0.46	0.85	0.35	0.55	0.04	1.20	0.32	2.85	0.72
Pr	3.71	1.37	1.57	0.21	0.81	0.16	0.34	0.13	0.18	0.01	0.36	0.06	0.56	0.16
Nd	25.97	11.37	10.40	1.89	9.58	1.77	3.86	1.29	1.79	0.09	3.39	0.53	3.43	1.05
Sm	9.58	4.21	4.51	0.96	7.79	1.23	3.24	0.64	1.77	0.08	2.53	0.36	1.73	0.63
Eu	3.34	1.37	1.83	0.38	3.79	0.48	1.52	0.29	1.13	0.05	1.35	0.14	0.80	0.27
Gd	11.48	4.02	6.86	1.42	17.28	2.05	7.03	1.41	4.94	0.23	5.20	1.17	3.65	1.04
Tb	1.59	0.51	0.83	0.13	3.06	0.33	1.10	0.21	0.89	0.04	0.86	0.12	0.41	0.12
Dy	11.38	3.39	5.63	0.72	21.04	2.31	8.15	1.44	5.58	0.19	5.60	0.89	2.45	0.66
Ý	126	15	155	25	654	81	352	55	183	6	186	28	123	15
Но	2.64	0.78	1.16	0.13	3.81	0.42	1.63	0.29	1.03	0.04	1.16	0.23	0.48	0.12
Er	8.94	2.82	3.79	0.55	8.95	0.99	4.38	0.75	2.49	0.09	3.42	0.93	1.24	0.27
Tm	1.37	0.49	0.57	0.06	0.83	0.09	0.46	0.08	0.26	0.02	0.44	0.18	0.14	0.03
Yb	9.71	3.56	4.57	0.62	4.39	0.54	2.81	0.54	1.53	0.06	3.22	1.56	0.84	0.17
Lu	1.33	0.53	0.68	0.10	0.48	0.06	0.32	0.06	0.20	0.01	0.50	0.26	0.12	0.02
TREE	235	49	208	29	738	90	388	61	206	7	215	33	143	16
HREE	163	26	172	27	697	85	371	58	195	6	201	31	129	15
HREE/TREE	0.70	0.06	0.83	0.02	0.94	0.00	0.96	0.01	0.95	0.00	0.93	0.01	0.90	0.03

Unit	BD	В	<b>.</b>		Δ			МНБ	PFO
Sample	CV15158	CV15127	CV15125	CV15020	CV15024	CV15026	CV16007	CV15002	CV15337
Analysis #	3	217	41	147	92	7	2	151	22
120	11.02	02.04	10.46	24.06	1F FC	10.07	10.57	10 17	2.00
La <sub>2</sub> O <sub>3</sub>	11.03	23.81	12.46	21.96	15.56	18.07	13.57	12.17	2.98
Ce <sub>2</sub> O <sub>3</sub>	32.82	33.17	35.12	32.94	32.21	31.86	31.68	31.29	24.33
Pr <sub>2</sub> O <sub>3</sub>	4.39	3.09	4.46	3.24	3.94	3.35	3.81	3.99	5.91
$Nd_2O_3$	16.61	8.99	13.12	9.29	13.35	11.74	13.86	12.97	26.84
Sm <sub>2</sub> O <sub>3</sub>	1.99	0.53	1.28	0.81	1.42	1.42	1.76	1.75	3.75
$Eu_2O_3$	0.45	-	-	-	0.19	-	0.40	0.36	0.73
$Gd_2O_3$	0.69	0.32	0.87	0.64	0.85	0.97	1.13	0.95	1.02
$Dy_2O_3$	-	-	-	0.21	-	-	-	-	-
$Y_2O_3$	0.24	0.24	0.46	0.38	0.41	0.32	0.75	0.48	0.51
ThO <sub>2</sub>	0.79	0.17	0.52	0.40	1.12	2.15	3.21	3.29	3.90
$UO_2$	_	_	_	_	-	_	_	_	_
CaO	0.84	0.30	0.99	0.20	0.14	0.46	0.63	0.99	0.52
$P_2O_5$	29.32	29.32	28.91	29.74	29.76	28.89	28.02	28.90	27.66
F	0.52	0.52	0.60	0.50	0.53	0.60	0.59	0.60	0.54
CI	-	-	-	-	-	-	-	-	-
SiO <sub>2</sub>	0.22	-	0.33	_	0.31	0.45	0.64	0.24	0.77
PbO	-	0.09	-	0.10	0.12	0.23	0.26	0.29	0.39
FeO	_	-	0.27	-	-	-	-	0.27	0.52
Na <sub>2</sub> O	_		_			_	_		_
SrO	0.25		0.17			0.16	0.27		0.44
Total	100.24	100.60	99.43	100.30	99.92	100.95	100.81	98.49	100.94
O=F	-0.22	-0.22	-0.25	-0.21	-0.22	-0.25	-0.25	-0.25	-0.23
Total	100.02	100.38	99.17	100.09	99.69	100.70	100.56	98.23	100.71
				Cations <sub>I</sub>	per 4 O				
La	0.161	0.347	0.183	0.319	0.226	0.264	0.200	0.180	0.044
Ce	0.474	0.480	0.511	0.474	0.464	0.462	0.465	0.460	0.359
Pr	0.063	0.044	0.065	0.046	0.056	0.048	0.056	0.058	0.087
Nd	0.234	0.127	0.186	0.131	0.188	0.166	0.198	0.186	0.386
Sm	0.027	0.007	0.018	0.011	0.019	0.019	0.024	0.024	0.052
Eu	0.006	0.001	0.002		0.003	0.002	0.005	0.005	0.010
Gd	0.009	0.004	0.012	0.008	0.011	0.013	0.015	0.013	0.014
Dy	0.001	0.001		0.003	0.002	0.002	0.002	0.002	0.003
Y	0.005	0.005	0.010	0.008	0.009	0.007	0.016	0.010	0.011
Ho	0.001					0.010			0.002
Th	0.007	0.002	0.005	0.004	0.010	0.019	0.029	0.030	0.036
U	0.000	0.040	0.040	0.000	0.000	0.040	0.001	0.001	0.000
Ca	0.036 0.980	0.012	0.042	0.009 0.990	0.006	0.019	0.027	0.043	0.022
P F	0.960	0.981 0.063	0.973 0.074	0.990	0.992 0.064	0.968 0.074	0.950 0.073	0.983 0.075	0.944 0.068
CI	0.003	0.003	0.074	0.061	0.004	0.074	0.073	0.075	0.003
Si	0.001	0.001	0.013	0.004	0.001	0.001	0.001	0.001	0.003
Pb	0.009	0.003	0.013	0.004	0.012	0.010	0.023	0.010	0.004
Fe	0.005	0.001	0.009	0.001	0.001	0.002	0.003	0.003	0.004
Na	0.000		0.000		0.001	0.000	0.000	0.000	0.010
Sr	0.006		0.004			0.004	0.006		0.010
Total	2.023	2.016	2.030	2.007	2.001	2.019	2.026	2.016	2.033
	-:- <b>-</b> -								

Unit	В	3D	В	Α	MHREO
Sample Analysis #	<b>CV15114</b> 75	<b>CV15115</b> 133	<b>CV15141</b> 88	<b>CV15004</b> 370	<b>CV15002</b> 348
La₂O₃	15.92	13.79	26.80	23.77	18.05
Ce <sub>2</sub> O <sub>3</sub>	36.46	35.87	36.81	34.90	34.80
$Pr_2O_3$	4.34	4.83	3.06	3.30	3.93
$Nd_2O_3$	12.99	14.72	7.96	9.04	11.55
$Sm_2O_3$	0.99	1.38	0.51	0.96	1.19
$Eu_2O_3$	-	_	-	_	_
$Gd_2O_3$	-	0.43	0.29	0.46	0.68
$Dy_2O_3$	-	_	_	_	_
$Y_2O_3$	0.26	0.21	0.19	0.37	0.49
ThO <sub>2</sub>	0.44	1.00	0.10	0.68	2.03
CaO	0.60	0.60	0.45	0.89	1.13
$P_2O_5$	-	_	0.25	-	_
F	8.22	7.93	8.06	8.86	7.97
CI	-	-	-	-	-
SiO <sub>2</sub>	0.35	0.34	0.16	-	-
PbO	-	-	-	-	-
FeO	-	0.26	-	-	0.29
SrO	0.08	0.07	40.50	0.16	0.23
CO₂ Total	22.33	21.45	18.52	19.90	20.35
O=F	100.00 -3.46	100.00 -3.34	100.00 -3.39	100.00 -3.73	100.00 -3.36
Total	96.54	96.66	96.61	96.27	96.65
	0.470	0.450	0.047	0.074	0.005
La Ce	0.173 0.394	0.153 0.395	0.317 0.432	0.274 0.399	0.205 0.393
Pr	0.047	0.053	0.432	0.038	0.044
Nd	0.137	0.158	0.091	0.101	0.127
Sm	0.010	0.014	0.006	0.010	0.013
Eu					
Gd		0.004	0.003	0.005	0.007
Dy	0.004	0.000	0.000	0.000	0.000
Y	0.004	0.003	0.003	0.006	0.008
Th Ca	0.003 0.019	0.007 0.019	0.001 0.015	0.005 0.030	0.014 0.037
P	0.013	0.013	0.013	0.000	0.007
F.	0.610	0.602	0.642	0.678	0.617
Si	0.010	0.010	0.005		
Fe		0.007			0.008
Sr	0.001	0.001		0.003	0.004
С	0.899	0.881	0.811	0.849	0.857

	Apatite, Mo Bastnas		Xeno	time	Tho	rite	Calcite, D Side	
	Standards	Counting Time (s)	Standards	Counting Time (s)	Standards	Counting Time (s)	Standards	Counting Time (s)
La	MAC-La	20			MAC-La	20		
Ce	MAC-Ce	20			MAC-Ce	20		
Pr	MAC-Pr	20			MAC-Pr	20		
Nd	MAC-Nd	20	MAC-Nd	20	MAC-Nd	20		
Sm	MAC-Sm	20	MAC-Sm	20	MAC-Sm	20		
Eu	MAC-Eu	20	MAC-Eu	20	MAC-Eu	20		
Gd	MAC-Gd	20	MAC-Gd	20	MAC-Gd	20		
Tb			MAC-Tb	20	MAC-Tb	20		
Dy	MAC-Dy	20	MAC-Dy	20	MAC-Dy	20		
Υ	MAC-Y	20	MAC-Y	20	MAC-Y	20		
Но	MAC-Ho	20	MAC-Ho	20	MAC-Ho	20		
Er			MAC-Er	20	MAC-Er	20		
Tm			MAC-Tm	20	MAC-Tm	20		
Yb			MAC-Yb	20	MAC-Yb	20		
Lu			MAC-Lu	20	MAC-Lu	20		
Th	ThO2	20	ThO2	20	ThO3	20		
U	UO2	20	UO2	20	UO3	20		
Ca	Apatite	20	Apatite	20	Apatite	20	Calcite	20
Р	Apatite	20	Apatite	20	Apatite	20		
F	Apatite	20	Apatite	20	Apatite	20		
Si	Diopside	20	Diopside	20	Diopside	20		
Cl	Vanadinite	20						
Pb	PbS	20	PbS	20	PbS	20		
Fe	Fe2O3	20	Fe2O3	20	Fe2O3	20	Siderite	20
Na	Albite	20			Albite	20	Albite	20
Sr	Sr_Feldspar	20					Sr_Feldspa	40
Ва	Ba_Feldspar	20					Ba_Feldsp	40
Mg	-						Dolomite	20
Mn							Siderite	20
Al							Garnet	20

Unit	Rim	CC 1	Rim CC 2	Rim DC	В	D	В	4	Ą
Type	Rim1-p	Rim1-s	Rim2	Rim3	BD-p	BD-s	В	А-р	` A-s
Sample	15029	15029	15049	15108	15114	15114	16010	15194	15193
Analysis	6-3	4	8-5	2-6	1-5	7-2	3B-3	1	2-3
La <sub>2</sub> O <sub>3</sub>	-	-	-	0.24	-	-	-	0.06	-
Ce <sub>2</sub> O <sub>3</sub>	0.19	0.23	0.29	0.37	0.23	0.35	0.28	0.30	0.25
Pr <sub>2</sub> O <sub>3</sub>	_	-	_	_	_	_	_	0.16	_
$Nd_2O_3$	0.16	0.22	0.16	0.17	0.30	0.35	0.22	0.15	0.27
Sm <sub>2</sub> O <sub>3</sub>	-	-	-	-	-	-	-	-	-
Eu <sub>2</sub> O <sub>3</sub>						_	_	_	_
Gd <sub>2</sub> O <sub>3</sub>	-	-	-	_	-	_	-		
	-	-	-	-	-	-	-	0.11	-
Dy <sub>2</sub> O <sub>3</sub>	-	-	-	-	- 0.47	-	- 0.47	-	0.16
Y <sub>2</sub> O <sub>3</sub>	-	-	-	-	0.17	0.18	0.17	0.29	0.58
Ho <sub>2</sub> O <sub>3</sub>	-	-	-	-	-	-	-	-	-
ThO <sub>2</sub>	-	-	-	-	-	-	-	-	-
$UO_2$	-	-	-	-	-	-	-	-	-
CaO	54.92	54.59	55.01	54.55	54.50	54.44	53.70	53.18	52.91
$P_2O_5$	41.50	41.83	41.65	41.79	41.51	42.20	41.85	40.98	42.06
F	3.79	3.88	3.27	4.59	4.33	3.46	3.95	3.89	3.95
CI	-	-	-	- 	-	-	-	- -	-
SiO <sub>2</sub>	-	0.14	0.19	0.13	-	-	-	0.18	-
PbO	-	-	-	-	-	-	-	-	-
FeO	-	-	0.15	-	-	-	-	0.05	-
Na <sub>2</sub> O	0.21	0.12	0.07	0.16	0.20	0.23	0.19	-	0.28
SrO BaO	0.49 -	0.42 -	0.64 -	0.47 -	0.63	0.53	1.81 -	0.79	1.43 -
Total	99.83	100.34	100.38	100.88	- 100.40	100.84	- 101.12	- 100.15	100.78
O=F,CI	-1.60	-1.63	-1.38	-1.93	-1.82	-1.46	-1.66	-1.64	-1.66
Total	98.23	98.70	99.00	98.95	98.58	99.38	99.46	98.51	99.12
TREO	0.35	0.45	0.44	0.79	0.70	0.87	0.66	1.08	1.25
				O = 12	2.5				
La				0.008				0.002	
Ce	0.006	0.00705	0.009	0.011	0.007	0.011	0.009	0.010	0.008
Pr								0.005	
Nd	0.005	0.0066	0.005	0.005	0.009	0.010	0.007	0.005	0.008
Sm									
Eu								0.000	
Gd Dy								0.003	0.004
Y					0.008	0.008	0.008	0.014	0.004
Ho					0.000	0.000	0.000	0.014	0.020
Th									
U									
Ca	4.986	4.93375	4.962	4.930	4.951	4.892	4.857	4.983	4.790
Р	2.978	2.9871	2.969	2.984	2.980	2.997	2.991	2.992	3.008
F	0.940	0.95635	0.814	1.114	1.062	0.855	0.973	1.117	0.973
CI		0.0404=	0.040	0.044				0.040	
Si		0.01215	0.016	0.011				0.016	
Pb Fe			0.011					0.004	
re Na	0.035	0.0198	0.011	0.025	0.032	0.038	0.031	0.004	0.046
Sr	0.033	0.0196	0.011	0.023	0.032	0.036	0.031	0.041	0.070
Ba	0.021	5.52500	3.001	5.020	5.001	5.020	2.000	5.511	5.0.0
	8.034	7.987	8.013	7.997	8.017	7.981	7.991	8.076	7.960

Unit	Mineral	δ13C V-PDB	δ18O V-SMOW
	calcite calcite	-5.44 -4.49	7.94 8.90
Rim CC 1	calcite	-5.22	8.89
	calcite calcite	-5.06 -5.33	9.53 7.73
	calcite	-5.35	8.47
Rim CC 2	calcite calcite	-5.46 -5.42	8.85 9.03
	calcite	-5.19	8.11
	calcite calcite	-5.38 -5.26	7.49 9.45
	calcite calcite	-5.07 -5.36	9.76 8.18
Rim DC	dol groundmass	-2.09	15.22
	dol groundmass dol groundmass	-0.49 -0.87	15.89 15.84
	dol groundmass	-1.96	15.68
	dol groundmass dol groundmass	-1.46 -1.19	12.99 15.17
	dol groundmass dol groundmass	-0.78 -0.60	15.45 16.41
	dol groundmass	-1.29	14.42
	dol groundmass dol 1	-1.17 -4.42	16.05 10.17
	dol 1	-4.62	9.57
	dol 1 dol 1	-4.44 -4.39	10.52 9.92
	dol 1 dol 1	-4.21 -4.29	10.86 9.14
	dol 1	-3.74	10.87
BD	dol 1 dol 1	-3.82 -3.96	10.21 10.74
	dol 1	-3.77	10.36
	dol 1 dol 1	-4.02 -3.53	9.95 10.62
	dol 1 dol 1	-4.56 -4.51	9.25 9.62
	dol 1	-4.48	9.20
	dol 1 dol 1	-4.32 -4.62	10.30 9.14
	dol groundmass dol groundmass	-3.28 -2.88	11.47 12.81
	dol groundmass	-3.04	13.95
	dol groundmass dol groundmass	-2.10 -2.20	15.44 15.42
	dol groundmass	-2.04	14.70
	dol groundmass dol groundmass	-2.65 -2.01	14.53 15.28
	dol groundmass dol groundmass	-2.89 -2.51	11.16 11.98
В	dol groundmass	-2.72	11.15
	dol dol	-2.62 -0.94	14.48 17.72
	dol dol	-2.94	10.34 14.83
	dol	-2.53 -3.01	10.00
	dol dol	-2.00 -2.63	16.34 14.89
	dol	0.26	17.00
	dol dol	-2.83 -2.86	12.10 14.41
	dol dol	-1.57 -1.49	17.47 15.15
	dol	-3.17	13.56
	dol dol	-2.72 -2.41	12.63 13.18
	dol dol	-1.97	15.79 14.40
	dol	-2.76 -1.81	16.95
	dol dol	-2.24 -2.78	13.84 11.93
	dol	-2.80	12.37
А	dol dol	-2.60 -2.68	12.16 15.41
	dol dol	-1.60 -2.37	17.54 15.57
	dol	-2.84	14.98
	dol dol	-2.44 -2.36	16.28 16.25
	dol	-2.32	15.47
	dol dol	-2.17 -1.91	16.90 15.39
	dol dol	-2.63 -2.37	15.82 15.00
MHREO	dol	-2.86	13.42
	siderite siderite	-2.49 -2.86	17.09 17.03
	siderite siderite	-3.73 -2.74	15.75 17.02
	siderite	-3.21	15.74
	siderite siderite	-3.33 -3.30	14.88 16.54
	siderite	-3.10	16.15
	siderite	-3.22	15.97